

Copyright

by

Hilary Elizabeth Strong

2009

**The Thesis Committee for Hilary Elizabeth Strong  
Certifies that this is the approved version of the following thesis:**

**The Origin and Properties of Mass Transport Deposits  
Ursa Basin, Gulf of Mexico**

**APPROVED BY  
SUPERVISING COMMITTEE:**

**Supervisor:**

---

Peter B Flemings

---

Ruarri Day-Stirrat

---

David Mohrig

**The Origin and Properties of Mass Transport Deposits  
Ursa Basin, Gulf of Mexico**

**by**

**Hilary Elizabeth Strong, BS**

**Thesis**

Presented to the Faculty of the Graduate School of

The University of Texas at Austin

in Partial Fulfillment

of the Requirements

for the Degree of

**Master of Science in Geological Sciences**

**The University of Texas at Austin**

**December 2009**

## **Dedication**

I dedicate this thesis to my fiancé, Dan Petrizzo, my parents, Michael Strong and Candace Person, and my sister, Emma Strong, for their exceptional love and support.

## **Acknowledgements**

I thank the Integrated Ocean Drilling Program Expedition 308 for seismic and LWD data, and core material. I thank the Jackson School of Geosciences and BP for financial support.

I thank also thank the following people: Derek Sawyer and Julia Schneider for advice, edits, data, and valuable discussions; Mark Andrews for laboratory support; John Germaine for assistance with data processing, trouble-shooting, and interpretations; Matthew Colbert for CT scanning and processing; and David DiCarlo for assistance in medical CT scanning.

I thank my committee members, Ruarri Day-Stirrat and David Mohrig for feedback to strengthen my thesis. I also thank Ruarri for providing SEM images and assistance in fabric analysis.

Lastly I thank my advisor, Peter Flemings, for his support, both academic and financial. From my two years working with Peter I have developed not only stronger scientific skills, but a stronger character as well. I have learned my potential extends far greater than I had previously thought, and with hard work, I am capable of great success.

November 11, 2009

## **Abstract**

### **The Origin and Properties of Mass Transport Deposits Ursa Basin, Gulf of Mexico**

Hilary Elizabeth Strong, MSGeoSci

The University of Texas at Austin, 2009

Supervisor: Peter B Flemings

Uniaxial consolidation experiments on Mass Transport Deposit (MTD) and non-MTD core samples from Ursa Basin, Gulf of Mexico, show MTDs have a lower porosity at a given effective stress compared to adjacent non-MTD sediments; a behavior observed in additional experiments on lab remolded Ursa core and resedimented Boston Blue Clay (BBC). I hypothesize debris flow action remolded the sediment: removing its stress history through shearing action, resulting in dense sediments at shallow depth. I supplement testing this hypothesis through lab remolding of BBC (in addition to Ursa clay) due to the greater availability and knowledge of this material. Ursa MTDs record multiple submarine slope failure events within the upper 200 meters below sea floor (mbsf); the most prominent is labeled MTD-2. MTDs have lower porosity and higher bulk density than surrounding, non-MTD, sediment. Porosity ( $\phi$ ) is 52% at 125mbsf – immediately below MTD-2; whereas  $\phi$  is 46% at 115mbsf – within MTD-2. Comparison of non-MTD samples to MTD-2 samples, and intact to remolded samples, shows a decrease in sediment compressibility ( $C_c$ ) within the MTD-2 and remolded sediments. Permeability within Ursa mudstones also declines with porosity according to:  $\log(k) = A\phi - B$ . Permeability is slightly higher within MTD-2; however grain size analysis indicates lower clay content in MTD-2 versus the non-MTDs. Pre-consolidation stress interpretations from the experiments show a linear trend in both MTD and non-MTD sediments, indicating both geologic units depict the same pore pressure profile. Remolding via debris flow explains the origin of MTDs at Ursa and governs the evolution of this geologic unit to its dense, highly consolidated, state today. At some point, slope failure triggered movement of the sediment down slope in form of a debris flow. The shearing action of the debris flow weakened the sediment, reducing its ability to support the overburden. As consolidation resumed, the remolded sediment followed a new, less steep,  $C_c$  curve. Within the geologic record, a distinctive dense, shallow unit is preserved; evidence for historical slope failure.

## Table of Contents

List of Tables .....	viii
List of Figures .....	ix
Chapter 1 The Origin and Properties of Mass Transport Deposits	
Ursa Basin, Gulf of Mexico .....	1
Introduction.....	1
Geologic Setting .....	3
Mass Transport Deposit Characteristics .....	5
Mass Transport Deposits and Uniaxial Consolidation .....	9
Uniaxial Consolidation Experiments .....	12
Intact Ursa Sediment .....	12
Synthetically Remolded Ursa Sediment .....	24
Resedimented Boston Blue Clay .....	28
Discussion .....	34
Conclusion .....	39
Appendix A Consolidation Experiments .....	42
Appendix B Grain Size Analysis .....	62
Appendix C Computed Tomography Core Scans.....	68
References.....	72
Vita .....	77

## **List of Tables**

Table 1:	CRS Results for Intact Specimens .....	13
Table 2:	Intact Specimen Overpressure .....	18
Table 3:	Permeability Results .....	20
Table 4:	Intact and Remolded Ursa CRS Results .....	27
Table 5:	Resedimented and Remolded BBC CRS Results .....	29
Table 6:	Nomenclature .....	41
Table A1:	Appendix Nomenclature .....	49
Table A2:	UT CRS Test Conditions and Consolidation Properties.....	50
Table A3:	Previous Ursa CRS Test Conditions and Consolidation Properties..	51



## List of Figures

Figure 1:	Bathymetric Map of Ursa Basin .....	4
Figure 2:	Ursa Seismic Cross Section .....	6
Figure 3:	LWD and Core Data of U1322 .....	7
Figure 4:	LWD, Seismic and Core Data from 40-130mbsf.....	8
Figure 5:	Medical CT Core Scans .....	10
Figure 6:	SEM Images.....	11
Figure 7:	Ursa Intact Consolidation Curves .....	14
Figure 8:	Ursa Permeability.....	21
Figure 9:	Ursa Grain Size versus Permeability .....	23
Figure 10:	Ursa Intact and Remolded Consolidation Curves.....	25
Figure 11:	BBC Intact and Remolded Consolidation Curves .....	32
Figure 12:	BBC Permeability .....	33
Figure 13:	Ursa MTD Evolution .....	38
Figure A1:	Pre-Consolidation Stress Interpretation Method.....	52
Figure A2:	Force Balance Analysis of Consolidation Experiments.....	53
Figure A3:	CRS016_ut Consolidation Data.....	54
Figure A4:	CRS017_ut Consolidation Data.....	55
Figure A5:	CRS018_ut Consolidation Data.....	56
Figure A6:	CRS021_ut Consolidation Data.....	57
Figure A7:	CRS037_ut Consolidation Data.....	58
Figure A8:	CRS038_ut Consolidation Data.....	59
Figure A9:	CRS039_ut Consolidation Data.....	60
Figure A10:	CRS040_ut Consolidation Data.....	61

Figure B1: BBC Intact and Remolded Consolidation Curves .....	65
Figure B2: BBC Permeability .....	66
Figure B3: Ursa MTD Evolution .....	67
Figure C1: Medical CT Core Scans .....	70
Figure C2: X-Ray CT Core Scans.....	71

# **Chapter 1: Exploring the Origin and Properties of Mass Transport Deposits, Ursa Basin**

## **INTRODUCTION**

Mass transport deposits (MTD) are the accumulated material of large-scale slides, slumps, and debris flows [Moscardelli *et al.*, 2006; Stow, 1986; Weimer and Shipp, 2004]. The Agulhas slide off South Africa is the world's largest known MTD and has a volume of approximately 20,000 km<sup>3</sup> [Dingle, 1977]. MTDs can form on slopes as steep as 25° in Seward, Alaska, or as shallow as 0.01° in the Mississippi delta [Hampton *et al.*, 1996].

Slope failure is caused by a reduction of effective stress (soil strength) or increase in shear stress [Davis *et al.*, 1983; Hubbert and Rubey, 1959; Iverson *et al.*, 1997]. Failure may be driven by earthquakes, excess pore water pressure build up from rapid sedimentation, oversteepening, abrupt sea level fall, surface wave loading, or geochemical changes [Coleman and Prior, 1988; Elverhøi *et al.*, 1997; Hampton *et al.*, 1996; Locat and Homa, 2002; Masson *et al.*, 2006]. MTDs develop in a variety of oceanic settings including continental margins, continental slopes, fjords, submarine canyons, and volcanic ridges and islands; and at any water depth [Hampton *et al.*, 1996; Prior *et al.*, 1984]. They can generate tsunamis, exacerbate coastal erosion, and destroy submarine infrastructure of the offshore oil and gas industry [Hornbach *et al.*, 2008; Locat and Homa, 2002; Masson *et al.*, 2006]. The penetration rate of gravity driven anchor piles and jetted conductors through MTDs can be twice as long as through non-MTD sediments [Shipp *et al.*, 2004]. This causes delays and adds cost to offshore drilling.

MTDs are highly deformed, chaotic units [Lucente and Pini, 2003; Martinsen and Bakken, 1990; Moscardelli et al., 2006; Sawyer et al., 2007b; Shipp et al., 2004; Weimer, 1990]. In outcrops, MTDs are preserved as inclined folds and antiformal duplex stacking, and random undeformed blocks amongst recumbent folds [Lucente and Pini, 2003; Martinsen and Bakken, 1990]. In seismic reflection data, MTDs are hummocky, mounded, chaotic, and contain subparallel reflections with variable amplitude and poor to fair continuity [Moscardelli et al., 2006; Sawyer et al., 2007b; Shipp et al., 2004; Weimer, 1990]. The base of an MTD in seismic data is recorded by a high amplitude, positive reflection that results from the strong density contrast between the MTD and immediately underlying non-MTD sediments [Moscardelli et al., 2006; Sawyer et al., 2007b]. Internally, the deposit is often semi-transparent, particularly in well-sheared zones with no undeformed blocks or extensional fault features [Posamentier and Kolla, 2003; Sawyer, 2009].

MTDs are part of the typical deepwater stratigraphic sequence [Moscardelli et al., 2006; Posamentier and Kolla, 2003]. In the Gulf of Mexico, this includes one or more MTDs at the sequence base (corresponding to the initial lowstand and rapid sedimentation), overlain by channel and levee deposits (corresponding to the late lowstand) [Moscardelli et al., 2006; Posamentier and Kolla, 2003]. Recent studies show the capping sequence (corresponding to the highstand) is often composed of an additional debris flow deposits [Moscardelli et al., 2006]. This indicates that MTDs can form in any sea-level conditions.

MTDs commonly have a higher density than surrounding, non-MTD sediments [Prior et al., 1984; Sawyer et al., 2007a; Shipp et al., 2004]. Debris flow densification is well documented and several studies confirm that the densest section of an MTD is

within the basal shear zone [*Major and Iverson, 1999; Piper et al., 1997; Prior et al., 1984; Sassa et al., 2003; Shipp et al., 2004; Tripsanas et al., 2003*].

I examine the origin and evolution of Ursa MTDs by combining observations from seismic, core and LWD data, with uniaxial consolidation experiments. The initial exploration of MTDs centers on observations of their distinct characteristics in seismic, LWD data, and CT scans of the cores. Consolidation experiments give further insight into the evolution of Ursa sediments, notably the compression and permeability behavior of material both within and outside of the MTDs. The origin of Ursa MTDs is then explored through consolidation experiments on synthetically remolded shallow Ursa core and resedimented Boston Blue Clay (BBC) to compare deformed, MTD deposits, with intact sediment compression behavior (Appendix A). From this study, I hypothesize laboratory remolding simulates the shearing action of the MTD-generating debris flows at Ursa – fabric and stress history were removed, resulting in a weak, highly compressible sediment. Remolding via debris flow explains the origin of MTDs at Ursa and governs the evolution of this geologic unit to its dense, highly consolidated, state today.

## **GEOLOGIC SETTING**

The Ursa Basin, northern Gulf of Mexico (Figure 1), is on the continental slope, approximately 210 km (130 miles) south-southeast of New Orleans, Louisiana. The Late Pleistocene shelf, shelf-margin, and turbidite sediments, sourced from the ancestral Mississippi River, are part of a larger system: the Eastern Depositional Complex [*Flemings et al., 2008; Sawyer et al., 2007b; Winker and Booth, 2000*]. The deposition of this complex is associated with Late Wisconsinan North American continental glaciation during the last ~70 ka during Marine Isotope Stages (MIS) 1-4 [*Sawyer, 2009; Winker and Booth, 2000*].

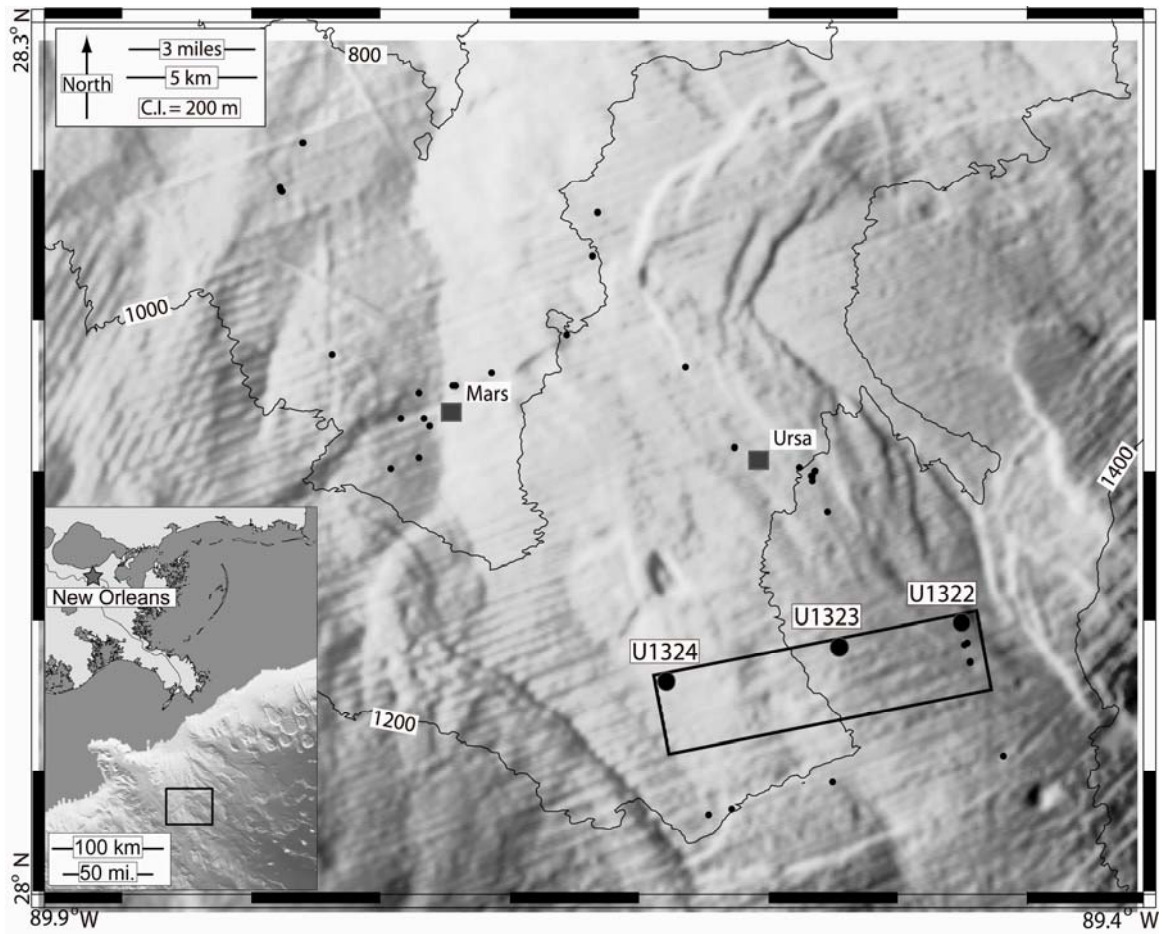


Figure 1: Bathymetric Map of Ursa Basin

IODP Expedition 308 Site U1322 is at 1300m water depth and Site U1324 is at 900m water depth. The two drill sites are 10km apart. The inset image shows the proximity of Ursa Basin (box) to New Orleans, Louisiana (star). Ursa is approximately 210km south-southeast.

This study centers on a series of ten MTDs at Ursa within the upper 600 meters below sea floor (mbsf) that are seismically imaged and penetrated at three drill sites by IODP Expedition 308 (Figure 2). MTD-1 and MTD-2 are laterally extensive, spanning all drill sites. MTD-3 through MTD-10 are smaller stacked events localized at U1322. Site U1322 is at a water depth of 1300m (4300ft); at this location core and logging-while-drilling (LWD) data extend to over 200 mbsf. Site U1324 is at a water depth of 800m (2624ft), with core and LWD data extending over 600 mbsf. No core was taken from Site U1323; however LWD data was collected to 247 mbsf. I focus on the physical properties and consolidation characteristics of MTD-2 at Site U1322.

### **MASS TRANSPORT DEPOSIT CHARACTERISTICS**

Ursa MTDs are imaged seismically as semi-transparent zones with prominent basal reflectors (Figure 2) [Sawyer *et al.*, 2007b]. The data derived from logging, and the shipboard moisture and density data show each MTD has a higher bulk density than surrounding, non-MTD material (Figure 3). The most striking example of this is the 5% increase in porosity of non-MTD material immediately below MTD-2 at 126mbsf (Figure 4). Undrained shear strength, as measured with a vane shear device, is also greater within the MTDs (Figure 3, 4). Resistivity is higher within MTD-2 than in the non-MTD sediments below, reflecting the lower porosity present.

Gamma ray LWD data indicate a homogenous lithology within MTD and non-MTD material. However, grain size analysis (Figure 4, Appendix B) from both this study and previous work on the Ursa samples, shows a slightly lower clay fraction (and higher silt fraction) in the MTD-2 cores than in the non-MTD cores [Sawyer *et al.*, 2007a].

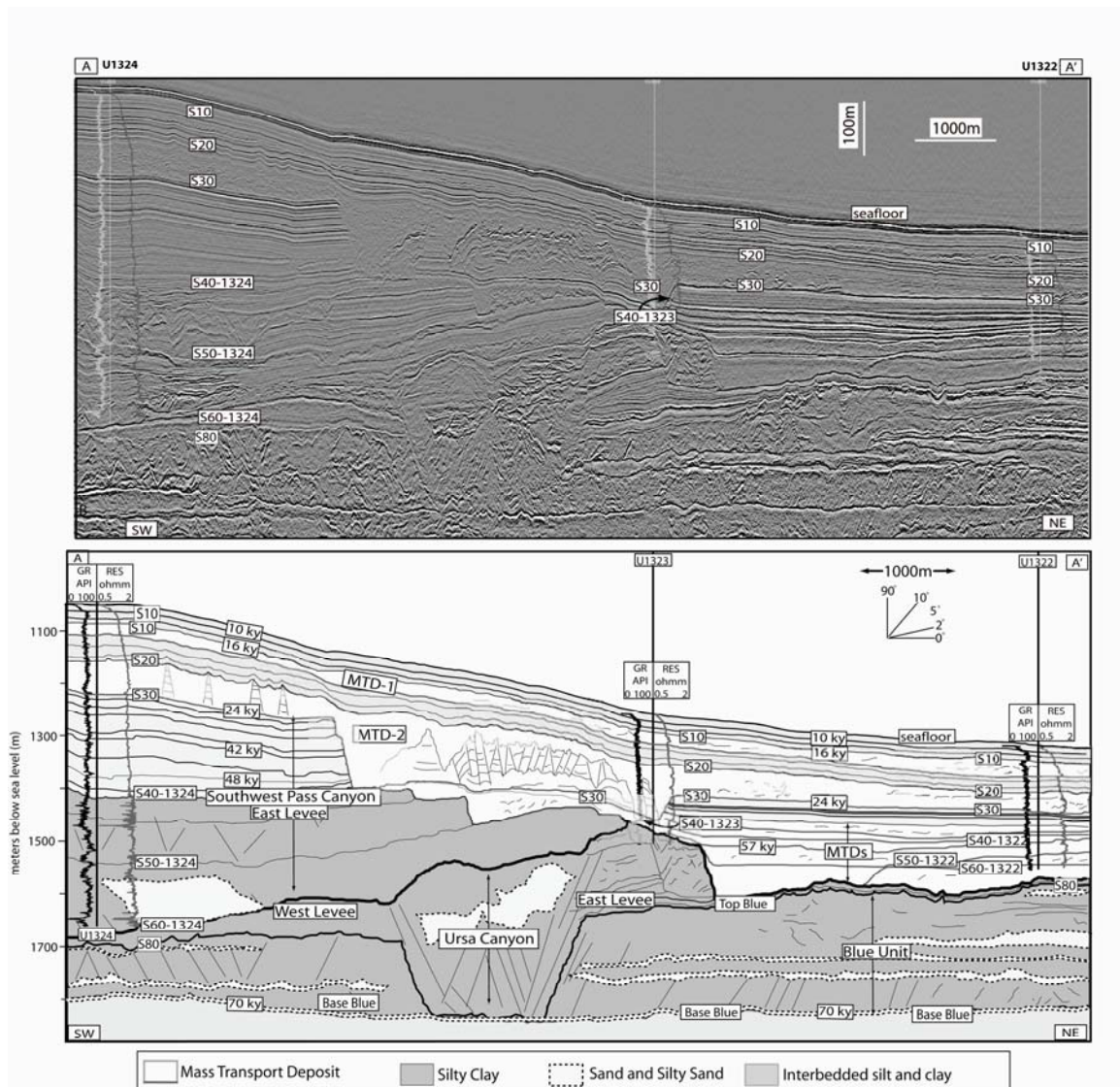


Figure 2: Ursa seismic cross section

Raw (top image) and interpreted (bottom image) seismic cross section of Ursa Basin (Sawyer et al 2009). MTDs are identified in the raw seismic data as internally transparent units with strong, positive, basal reflections. MTDs are colored in white in the interpreted seismic cross section. From this figure it is evident that MTD-2 is the largest and most laterally extensive.



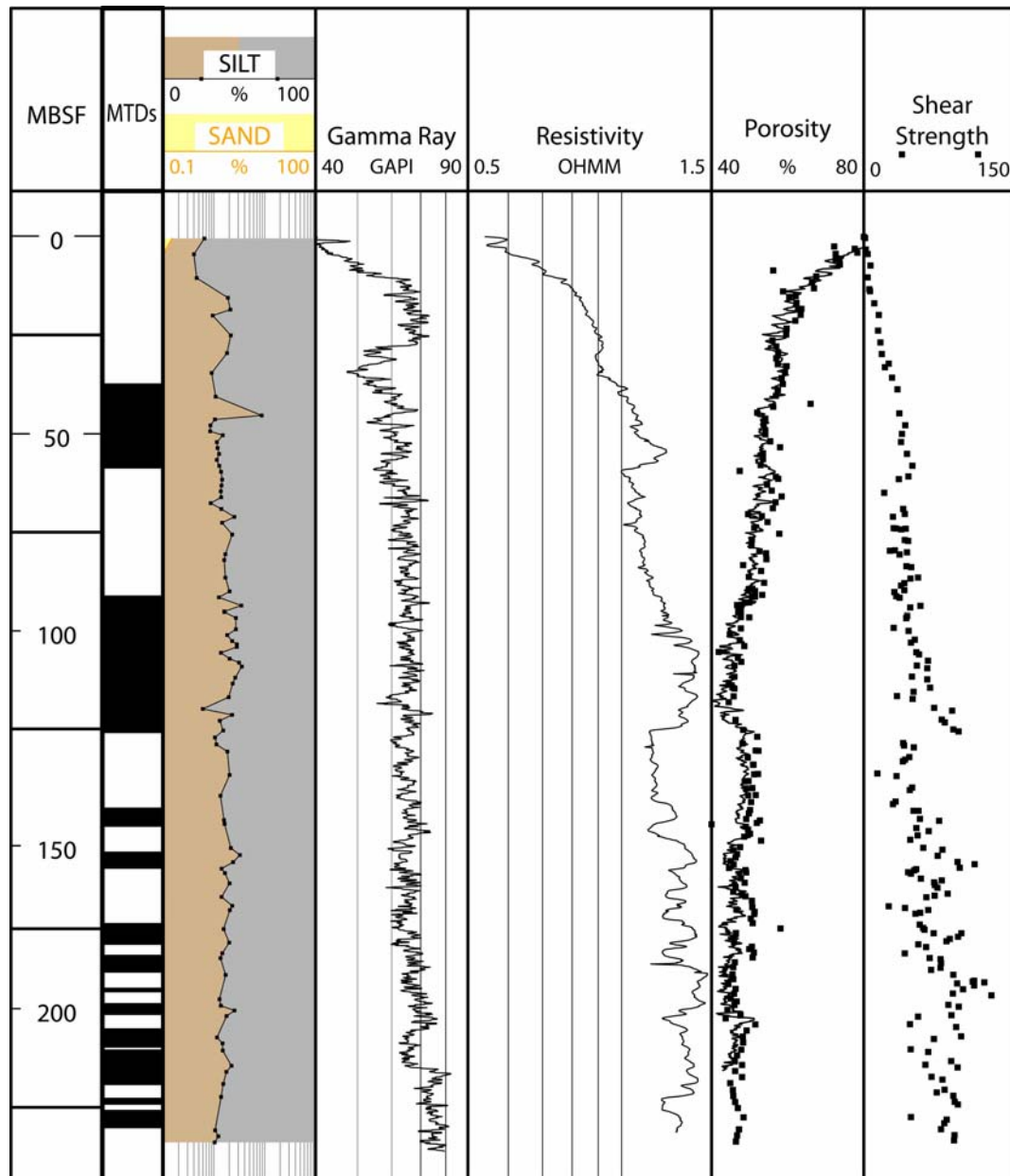


Figure 3: LWD and Core Data of Site U1322

Black rectangles in the MTDs column denote presence of an MTD. The grain size column shows silt in brown and clay in gray from a previous study (Sawyer et al, 2008). The gamma ray lithology log matches well with grain size. There is a distinct increase in resistivity and shear strength within MTD-2, corresponding to decrease in porosity. Note the abrupt increase in porosity from the base of MTD-2 to non-MTD sediments immediately below. Porosity is calculated from LWD bulk density (line) and shipboard moisture and density measurements (squares) using grain density = 2.74g/cc and pore fluid density = 1.023g/cc.

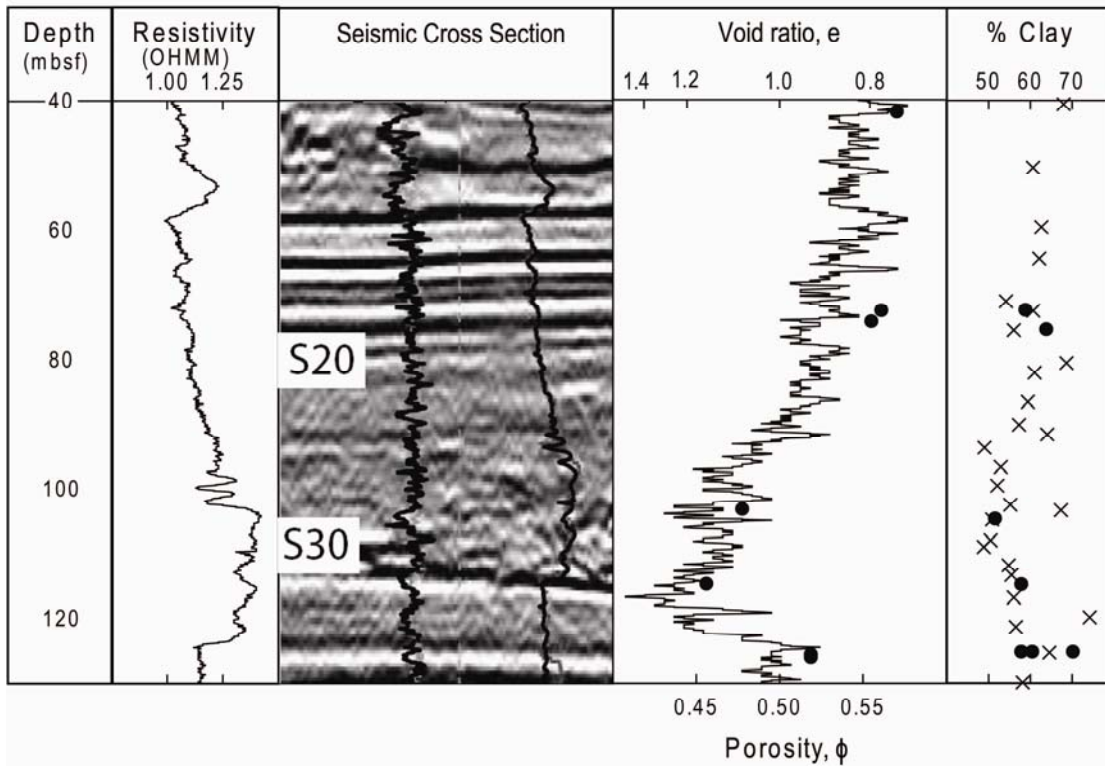


Figure 4: LWD, Seismic, and Core Data from 40-130 mbsf

This study focuses on cores from 40 to 130 mbsf. Consolidation experiments in this interval are denoted by a black circle. In the void ratio column, the circle refers to the void ratio measured from the specimens. The void ratio line is from LWD data. In the % clay column, the circle refers to the grain size determined (see Appendix B). The crosses in the % clay column are from a previous grain size analysis study on U1322 cores [Sawyer *et al*, 2007]. MTD-2 is identified by increased resistivity and decreased porosity.

Computed Tomography (CT) scans show that the MTD-2 core is very deformed with respect to non-MTD core (at a depth location immediately below MTD-2) (Figure 5, Appendix C). The MTD-2 core, 13H6 (Figure 5a), has no coherent sections of material; rather, it displays sections of sheared bedding, and multiple fine fractures propagating throughout. Intact sections of the non-MTD core, 15H1 (Figure 5b), show smooth, homogenous silty-clay, with no evidence of shearing.

Scanning Electron Microprobe (SEM) images of MTD and non-MTD sediments show a stark fabric contrast on a micrometer scale (Figure 6). The non-MTD sample (Figure 6a and 6c) has no apparent clay mineral alignment, and ample pore space around the larger quartz minerals. In contrast, the MTD sample (Figure 6b and 6d) appears to have a stacked, parallel alignment of clay aggregates, many of which wrap around the larger quartz grains, closing off pore space. These SEM images qualitatively indicate a different fabric and stronger grain alignment in MTD than non-MTD sediments.

### **Mass Transport Deposits and Uniaxial Consolidation**

The dominant strain in basin settings is vertical, thus uniaxial consolidation laboratory tests serve as a good analogue to geologic consolidation [Feeser *et al.*, 1993; Karig and Hou, 1992; Stump and Flemings, 2002]. Several studies use consolidation tests on core samples from MTDs to determine disturbance and stress history [Long, 2008; Piper *et al.*, 1997; Saffer, 2003; Stump and Flemings, 2002]. To analyze the consolidation characteristics of sediments at Ursa, I conducted Constant Rate of Strain (CRS) uniaxial consolidation tests on intact core specimens from Site U1322 above, below, and within MTD-2. I also conducted CRS tests on synthetically remolded core specimens from above MTD-2. CRS tests yield stress-strain behavior of soil. These experiments document the change in porosity due to change in effective stress

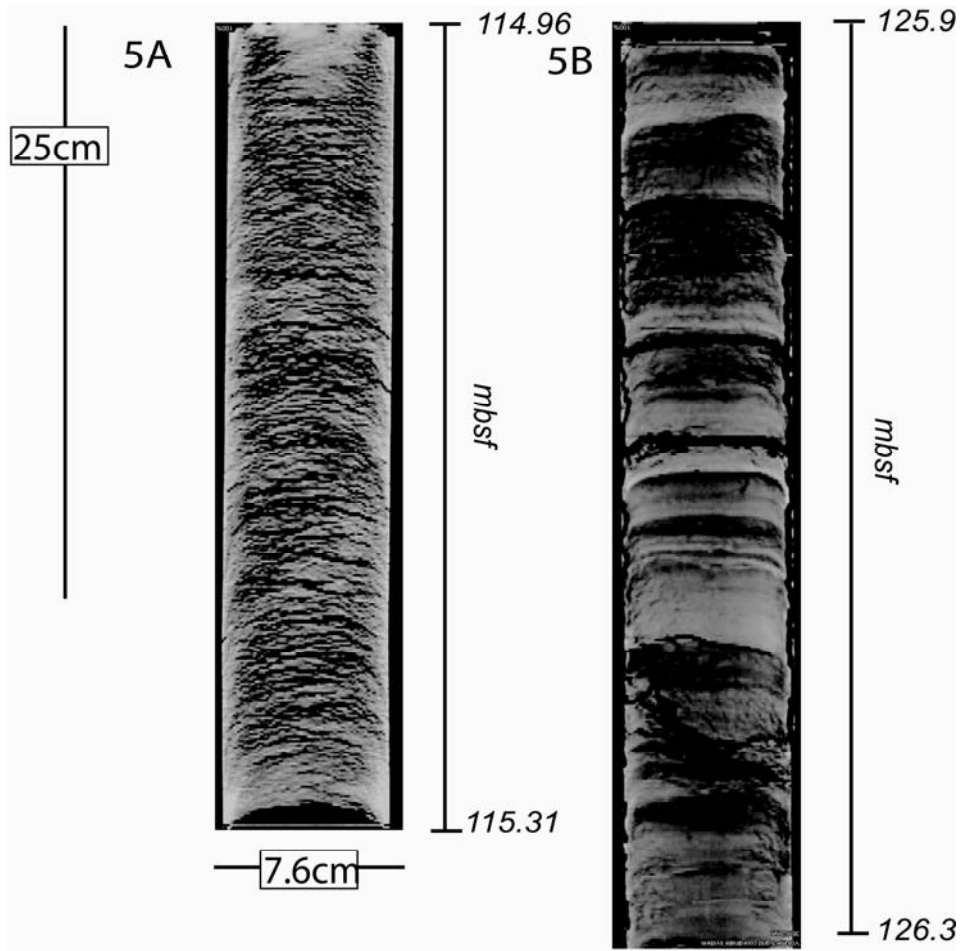


Figure 5: Medical CT Core Scans

The following scanning parameters were used to obtain the CT images: 1mm slices, 120kV, 100mA, and 4 second scan time. The cores are processed with a gray density scale where black is air and white is high density material. 5a is within MTD-2 at 115mbsf and shows a myriad of fine fractures throughout the core. 5b is located immediately below MTD-2 at 126mbsf. The intact sections of 5b show smooth, homogenous material. The large cracks are due to dehydration and coring process.

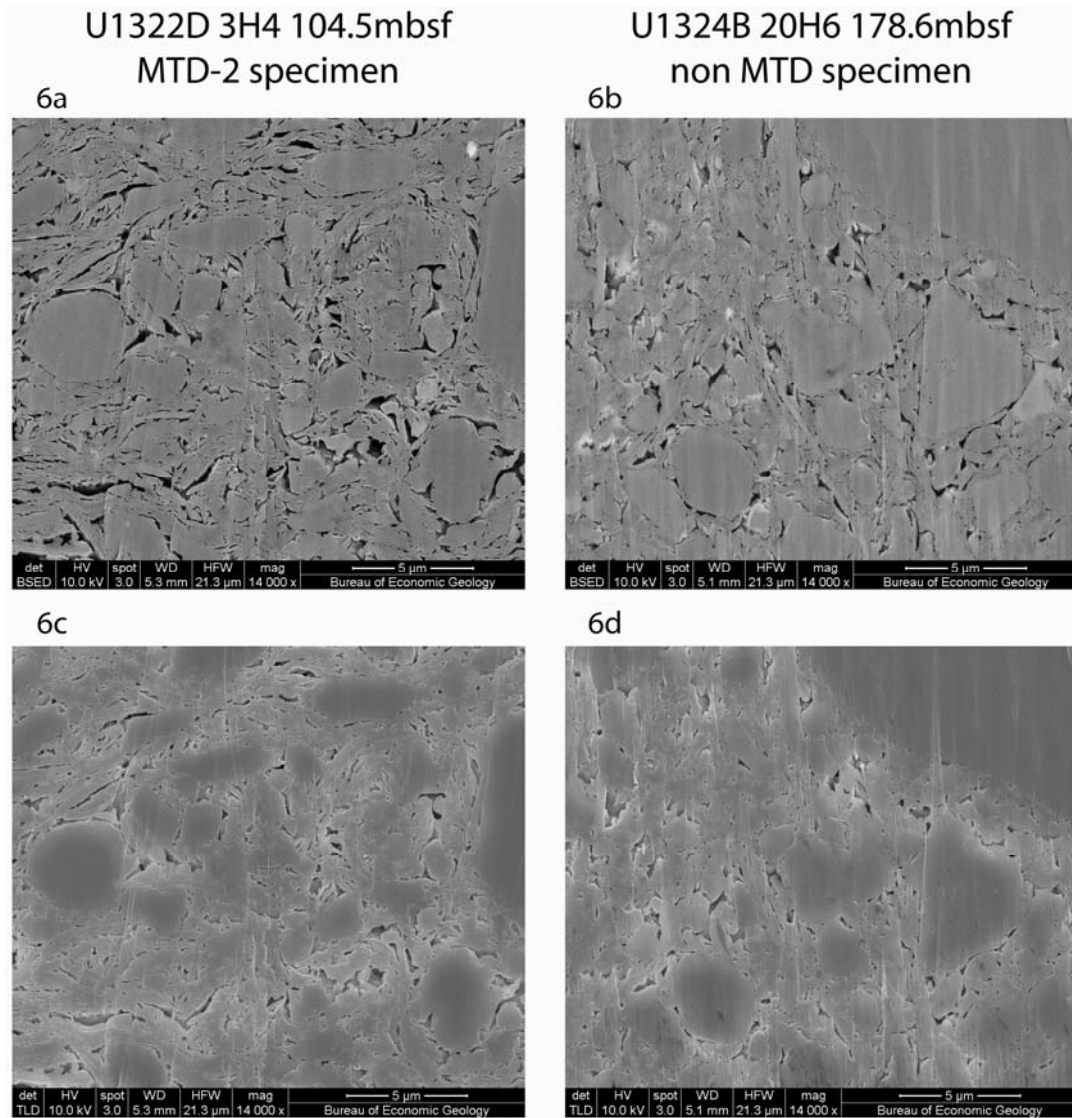


Figure 6: SEM images

These images are captured using a backscattered electron detector (6a and 6b) and secondary electron detector (6c and 6d). Clay minerals in the MTD-2 images (6a and 6c) wrap around the larger quartz grains. Clay minerals in the non-MTD images (6b and 6d) show more random alignment. This indicates remolding induces a different sediment fabric. The preparation process prevents determining orientation of the images.

[4186, 2006; *Lambe and Whitman*, 1969]. From this test it is possible to obtain coefficient of consolidation ( $C_v$ ), consolidation index ( $C_c$ ), swelling index ( $C_s$ ), Pre-consolidation stress ( $P'_c$ ), hydraulic conductivity ( $K$ ), and permeability ( $k$ ). Consolidation studies are limited; drilling disturbance increases with depth of penetration, and is far greater in submarine environments than subaerial environments due to added complications of the overlying water column [*Feesser et al.*, 1993].

## UNIAXIAL CONSOLIDATION EXPERIMENTS

### Intact Ursa Sediments

I ran consolidation tests on three intact cores: CRS016\_ut at 75 mbsf (non-MTD), CRS017\_ut at 115 mbsf (MTD-2), and CRS018\_ut 126 mbsf (non-MTD, immediately below MTD-2) following the method of ASTM 4186 (2006) (Table 1). The specimens were back-pressured to 386 kPa, consolidated at a constant strain rate to 3800 kPa effective stress, and then completely unloaded at 50% of the initial strain rate (Appendix A). Many of the tests included an unload-reload cycle, beginning at 5 or 10 times the expected pre-consolidation stress ( $P'_c$ ). I compared the results to a previous CRS study [*Long*, 2008] on Ursa Site U1322 cores of similar depths: CRS796\_mit at 73 mbsf (non-MTD), CRS021\_rice at 104 mbsf (MTD-2), and CRS808\_mit at 126 mbsf (non-MTD, immediately below MTD-2) (Figure 7, Tables 2 and 3).

### Ursa Results

The consolidation curves from these experiments are shown in Figure 7. CRS796\_mit and CRS016\_ut are non-MTD cores above MTD-2 at 73 mbsf and 75 mbsf, respectively (Figure 4, Table 2). CRS021\_rice and CRS018\_ut lie within MTD-2 at 104 mbsf and 115 mbsf. CRS808\_mit and CRS017\_ut are from the same 126 mbsf

<b>Experiment</b>	<b>Depth (mbsf)</b>	<b>Unit</b>	<b>e</b>	<b><math>\phi</math></b>	<b>P'<sub>c</sub> (kPa)</b>	<b>C<sub>c</sub></b>	<b>C<sub>s</sub></b>
CRS016_ut	74.5	Non-MTD	1.24	0.55	250	0.5223	0.1682
CRS018_ut	114.56	MTD-2	0.82	0.45	275	0.2217	0.0762
CRS017_ut	125.8	Non-MTD	1.04	0.51	330	0.3792	0.1059
CRS796_mit	72.8	Non-MTD	1.28	0.56	280	0.4675	0.1114
CRS021_rice	103.4	MTD-2	0.96	0.49	274	0.2749	0.0727
CRS808_mit	126.3	Non-MTD	1.07	0.52	516	0.3123	0.0500

Table 1: CRS Results for Intact Specimens

Data for uniaxial consolidation experiment conducted on intact Ursa specimens at the UT GeoMechanics laboratory and from a previous study [Long *et al.*, 2008]. Void ratio (e) and porosity ( $\phi$ ) are measured from the specimen. Pre-consolidation stress (P'<sub>c</sub>) is interpreted from the consolidation curve (described in Appendix A). The compression and swelling indices (C<sub>c</sub> and C<sub>s</sub>) are the loading and unloading slopes on a log stress vs void ratio curve. C<sub>c</sub> is measured over the virgin consolidation curve (flat section); C<sub>s</sub> is measured from the maximum stress (3800 kPa) to an unloading stress of 500kPa.

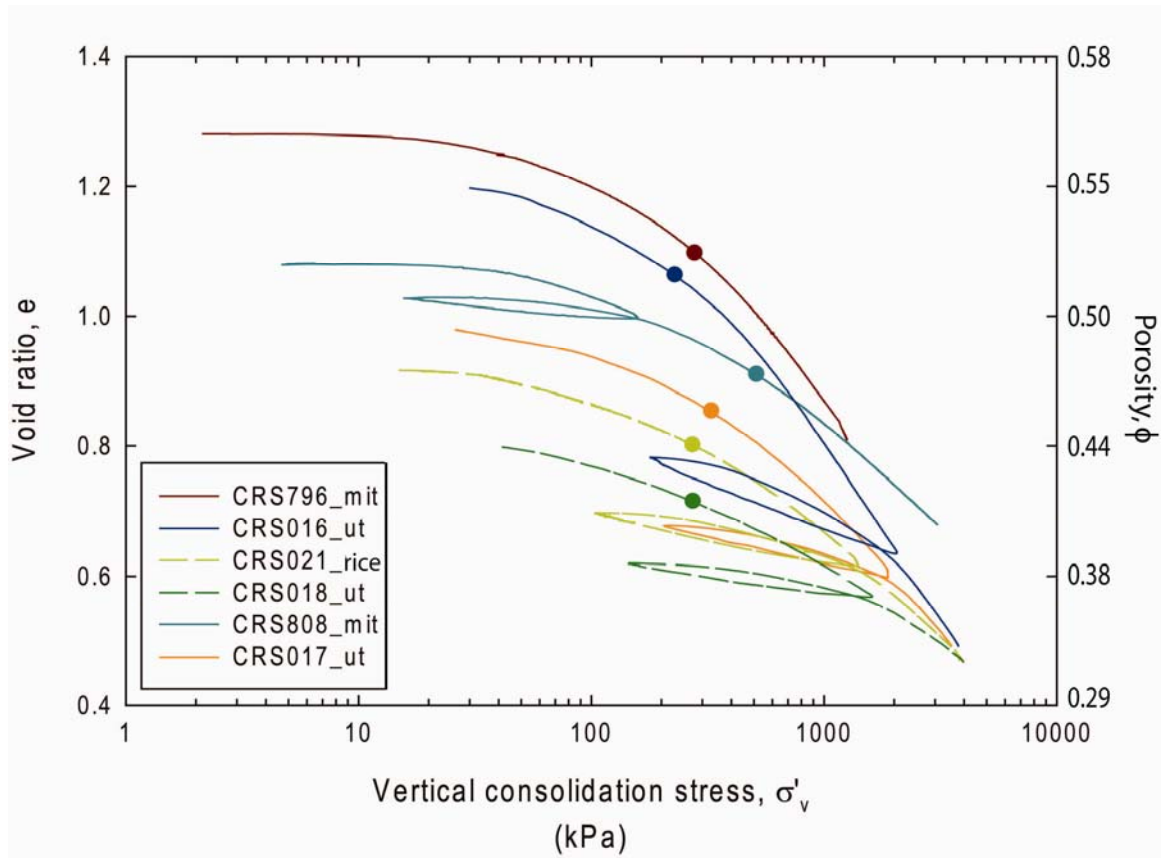


Figure 7: Ursa Intact Consolidation Curves

Specimens located within MTD-2 are denoted as dashed lines, whereas the non-MTD specimens are depicted with solid lines. The solid circles show the Pre-consolidation stress as interpreted by Becker et al's (1987) method. These values are actually relevant to the in situ void ratio, however are plotted on the curve intersection for easier association. This figure illustrates the low porosity of MTD-2, and that  $P'_c$  is a function of depth. Table 1 summarizes data associated with these consolidation curves.



core and represent non-MTD material located immediately below MTD-2. The consolidation results are compared and contrasted by similar depth and whether they are in MTD-2 or a non-MTD unit. Results are summarized in Tables 1, 2, and 3.

The in situ void ratio of the six specimens is highest within the two shallow non-MTD specimens and lowest in the two MTD-2 specimens (Table 1, Figure 4). The core-measured porosity values (circles in Figure 4) all lie about 2 to 5 porosity units above the porosity that is calculated from the LWD bulk density log. I interpret that core expansion during core recovery is the cause of this discrepancy. CRS796\_mit and CRS016\_ut are the non-MTD specimens located above MTD-2 at 73 and 75mbsf. The specimens have void ratios of 1.28 and 1.24, corresponding to porosities of 56.1% and 55.3%, respectively. CRS808\_mit and CRS017\_ut are also non-MTD sediments; however these are below MTD-2 at 126mbsf. The void ratios of these specimens are lower at 1.08 and 1.04, corresponding to porosities of 51.9% and 51.0% (Table 1). Despite not being from the greatest depth, the MTD-2 specimens, CRS021\_rice from 104mbsf and CRS018\_ut from 115mbsf, have the lowest void ratios at 0.96 and 0.82, respectively (porosity = 49.0% and 45.0%) (Table 2). Thus, the MTD-2 specimens are more densified than non-MTD specimens from greater depth. In sum, both core measurements and LWD calculations document a decrease in MTD-2 porosity by as much as 10 porosity units, with respect to non-MTD sediments at Ursa.

Compression indices,  $C_c$ , range from 0.2217 to 0.5223, and are lowest in MTD-2 (Table 1; Figure 6). Swelling indices,  $C_s$ , at U1322 range from 0.0269 to 0.1682.  $C_c$  is calculated as the slope of void ratio vs. log effective stress for plastic deformation.  $C_s$  is calculated as the unload slope (measured from 3800kPa to 500kPa effective stress).  $C_c$  values decline with decrease in porosity, irrespective of location with MTD or non-MTD

sediments (Figure 6, Table 2). The trend for the intact experiments of this study is  $C_c = 2.1\phi - 0.75$ ; the trend for intact experiments of this study combined with other U1322 experiments [Long, 2008] is  $C_c = 2.7\phi - 1.05$ . There is no clear trend between swelling indices,  $C_s$  and porosity.  $C_s$  is typically 1/5 to 1/10 of  $C_c$  [Das, 2002]; the average ratio for Ursa is 1/4 for both MTD and non-MTD samples, indicating a greater ability for this material to swell.

Pre-consolidation stress ( $P'_c$ ) values for each CRS test are interpreted by plotting Work against Vertical Effective Stress (Table 1) [Becker *et al.*, 1987]. In this approach  $P'_c$  is defined as the intersection of the slope of work from the initial plastic curve and the slope of work from the elastic curve (Appendix A). The shallow non-MTD specimens, CRS796\_mit and CRS016\_ut, have  $P'_c$  values of 280 and 250 kPa. The MTD-2 specimens, CRS021\_rice and CRS018\_ut, have  $P'_c$  values of 274kPa and 275kPa. The two specimens immediately underlying MTD-2, CRS017\_ut and CRS808\_mit, have  $P'_c$  values of 330 and 516 kpa, respectively (Table 1). The large discrepancy in CRS017\_ut and CRS808\_mit is particularly unusual given that the specimens are from the same core.

An ideal compression curve shows a strong transition from elastic consolidation (shallow slope) to plastic consolidation (steep slope) on a void ratio versus log effective stress plot. The pronounced rollover from reloading to virgin consolidation curve, as opposed to sharp transition, indicates sample disturbance and results in a  $P'_c$  estimation that may be less than actual in situ conditions [Olson, 1986]. Interpreting  $P'_c$  from IODP cores is particularly difficult because the 10m piston core used for sample retrieval induces a high degree of disturbance in the specimens [Dugan *et al.*, 2003].

Piston-core disturbance is visible within the CT scans (Figure 5) as the downward curve in bedding along the core edge. This effect is more prominent in the MTD-2 core

(Figure 5a) than the non-MTD core (Figure 5b), indicating greater deformation. As sediment density increases, the difficulty of extracting the core sample increases, resulting in greater disturbance. From LWD and core data (Figure 3 and 4), MTD-2 is the densest sediment in this study, and therefore would be most difficult to core.

Debris flow-induced remolding provides an additional source of disturbance to the sediment structure. Therefore the great degree of curve rounding observed within the MTD-2 compression curves may explained by soil disturbance from both coring and remolding.

Pre-consolidation stress is used as an estimate for in situ effective stress, assuming the current stress conditions are the maximum the rock has experienced in geologic history. From  $P'_c$  and total vertical stress ( $\sigma_v$ ), pore pressure ( $u$ ) is calculated from Equation 1:

$$u = \sigma_v - P'_c \quad (1)$$

Total vertical stress ( $\sigma_v$ ) is calculated by integrating the bulk density log from the seafloor to the appropriate depth. From equation 2, I then calculate the overpressure ratio ( $\lambda$ ), defined as:

$$\lambda^* = \frac{u - u_h}{\sigma_v - u_h} \quad (2)$$

The hydrostatic pressure ( $u_h$ ) is calculated using a ship-measured 1.023g/cc pore fluid density. The results of this study yield an average 0.63  $\lambda^*$ , with a range of 0.56 to 0.73; both studies averaged yield 0.57  $\lambda^*$  (Table 2). MTD-2 experiments average overpressure ratio is 0.65; somewhat high, but within the range for this region. The greater degree of rounding a from these two compression curves likely explain the low estimate of  $P'_c$  and thus higher  $\lambda^*$ .

Experiment	Depth (mbsf)	e	$\sigma_v$ (kPa)	$\sigma'_v$ (kPa)	$P'_c$ (kPa)	$P'_c$ min (kPa)	$P'_c$ max (kPa)	$\lambda^*$ ( $P'_c$ )
CRS796_mit	72.8	1.28	1243	210	280	--	--	0.45
CRS016_ut	74.5	1.24	1274	210	250	235	300	0.56
<b>CRS021_rice</b>	<b>103.4</b>	<b>0.96</b>	<b>1789</b>	<b>300</b>	<b>274</b>	--	--	<b>0.64</b>
<b>CRS018_ut</b>	<b>114.56</b>	<b>0.82</b>	<b>1994</b>	<b>330</b>	<b>275</b>	<b>220</b>	<b>300</b>	<b>0.67</b>
CRS017_ut	125.8	1.04	2200	375	330	318	390	0.65
CRS808_mit	126.3	1.07	2206	375	516	--	--	0.45

Table 2: Intact Specimen Overpressure

Data are presented for each consolidation experiment run from this study and Long et al. [2008] from 70 mbsf to 130 mbsf. The bolded experiments, CRS021\_rice and CRS018\_ut are from within MTD-2. All other experiments are not within an MTD. As with Table 1, e represents initial sample void ratio. Vertical stress ( $\sigma_v$ ) and effective stress ( $\sigma'_v$ ) do not account for the overlying water column, since this is not reproduced in the consolidation experiments.  $P'_c$  is interpreted from the consolidation curves as described in Appendix A. A minimum and maximum are provided to indicate a range of values is possible.  $\lambda^*$  is calculated from equations 1 and 2.

Flemings et al [2008] documented an approximately linear increase in pore pressure with depth over the first 200mbsf, corresponding to a  $\lambda^*$  of 0.6. Averaged  $\lambda^*$  for both this study and Long et al. [2008] is 0.57, indicating pre-consolidation stresses from CRS experiments do serve as a good proxy for in situ pressure conditions. The slightly higher overpressure ratio (0.65) from MTD-2 experiments may reflect an actual increase in overpressure from this unit, or could reflect sample disturbance. Ultimately, these results also confirm the increased density in MTD-2 cannot be explained by an increase in effective stress.

CRS experiments also yield data to calculate permeability during consolidation. Log permeability within each specimen declines linearly with porosity according to:

$$\log(k) = A \phi - B \quad (3)$$

The virgin consolidation data are plotted (Figure 8) and a best-fit linear regression trend is calculated for each experiment (Table 3). Using the initial specimen porosity ( $\phi$ ), in situ permeability values are calculated (Table 3).

Permeability trends are highest within the MTD-2 experiments, CRS021\_rice and CRS018\_ut, when plotted as void ratio versus log permeability (Figure 8). Permeability trends are lowest within the two shallow non-MTD specimens (CRS796\_mit and CRS016\_ut). The deepest specimen permeability trend, non-MTD CRS808\_mit, falls between both sets. Ideal conditions for calculating permeability are maintaining excess pore pressures of 5 to 12% during the CRS experiment, according to ASTM 4186 [2003]. CRS016\_ut and CRS796\_mit both fall within this range, all of the other experiments fall below (Appendix A). Grain size can also affect permeability. For this study and Long et al. [2008] grain size analyses show the MTD-2 has a higher silt fraction (Figure 9, Table 3), than the more clay dominate non-MTD specimens. Thus the higher permeability in

Experiment	Depth (mbsf)	e	$\phi$	% Clay	Permeability log (k) ( $m^2$ )	In Situ Perm (k) ( $m^2$ )
CRS796_mit	72.8	1.28	0.56	59	--	1.46E-17
CRS016_ut	74.5	1.24	0.55	64	10.21x – 22.83	6.32E-18
<b>CRS021_rice</b>	<b>103.4</b>	<b>0.96</b>	<b>0.49</b>	<b>52</b>	--	<b>2.27E-17</b>
<b>CRS018_ut</b>	<b>114.56</b>	<b>0.82</b>	<b>0.45</b>	<b>58</b>	<b>9.81x – 21.81</b>	<b>4.11E-18</b>
CRS808_mit	126.3	1.07	0.52	60	--	2.44E-17

Table 3: Permeability Results

Permeability data for each specimen are presented in reference to void ratio (e), porosity ( $\phi$ ) and % clay as determined in via grain size analysis (see Appendix B). MTD-2 specimens are again bolded. In situ perm is calculated from the in situ porosity and permeability trend equation. The trend is calculated from permeability data in the virgin consolidation stage of the experiment.

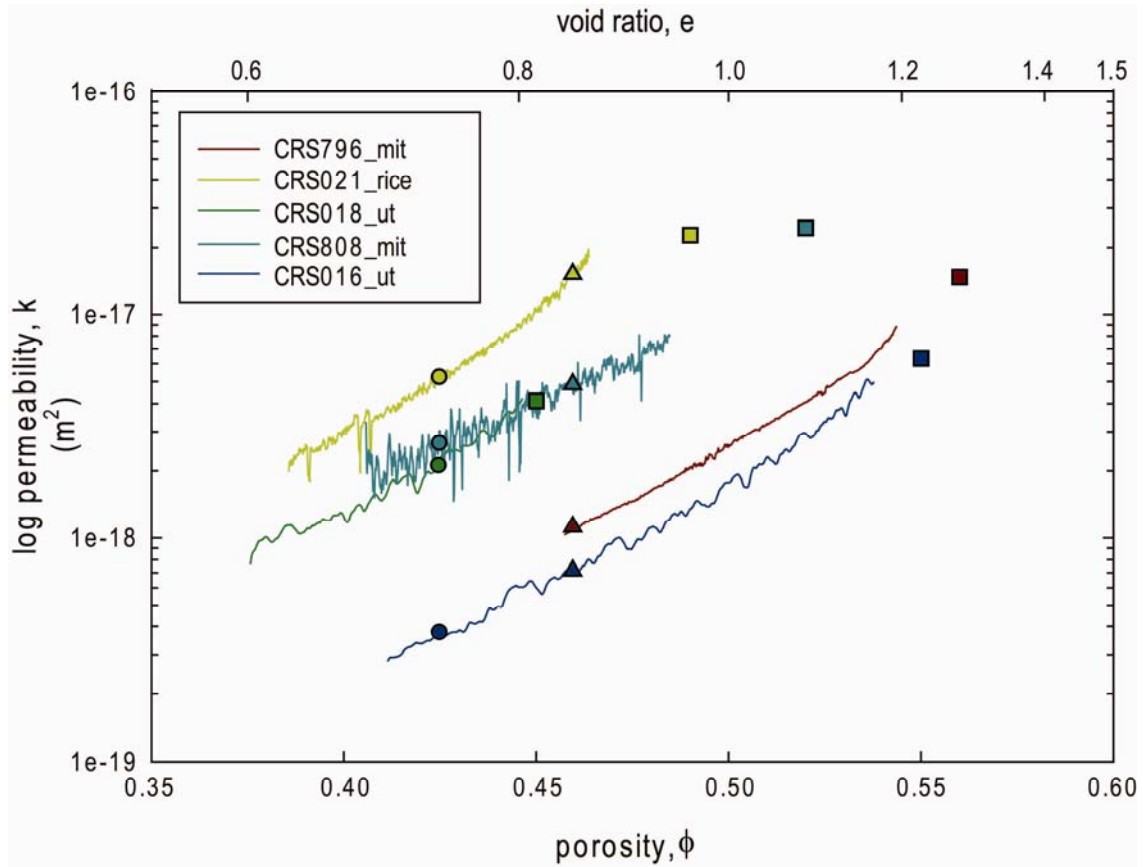


Figure 8: Ursa Permeability

Permeability trends of Ursa experiments show low permeability in the non-MTD specimens, particularly CRS796\_mit (72.5mbsf) and CRS016\_ut (75mbsf). Permeability is relatively higher within the MTD-2 specimens. The triangles and circles correspond to an analysis of grain size and permeability in Figure 9. The squares correspond to the in situ permeability of each specimen, as calculated from the interpreted  $\log(k) = A\Phi - B$  trends of Table 3.

MTD-2 may be due to coarser sediment composition or different experimental pore pressure conditions, and not reflect a distinction in MTD versus non-MTD.

### ***Intact Consolidation Curve Analysis***

Consolidation curves (Figure 7) indicate that at a given effective stress, MTD-2 porosity is much lower than non-MTD porosity, even comparing MTD-2 to non-MTD core from a greater depth. This behavior is expected due to the lower in situ porosity of MTD-2 as compared to non-MTD cores both above and below this unit. Since the in situ porosity dictates the curve starting point, the two highest curves correspond with the shallowest cores, followed by deep non-MTD cores, and lastly, the MTD-2 cores. While in situ porosity is affected by the debris flow, the pre-consolidation stress merely reflects the stress induced by the overburden. Thus while the MTD-2 curves are lowest on the plot, there is not a linear trend of increasing  $P'_c$  in situ porosity. Rather  $P'_c$  increases from shallow to deep non-MTD, and decreases from deep non-MTD to MTD-2.

The deep non-MTD samples have undergone a greater degree of consolidation due to geologic loading than the shallow non-MTD cores, thereby explaining the decline in porosity. However, remolding causes the porosity to decline even further in MTD-2 than in deep non-MTD specimens. As the in situ porosity declines, so does  $C_c$ , indicating a diminishing ability of the specimen to consolidate, even under great effective stress. Despite the great difference in initial void ratio, nearly all of the experiments seem to converge at a void ratio of 0.55 at the highest consolidating stress of 3800kPa (Figure 7).

The discrepancy in void ratio of MTD-2 versus non-MTD specimens is greatest at lower effective stresses (a few hundred kPa); however the consolidation curves converge at the maximum effective stress of the experiment (3800kPa). I hypothesize



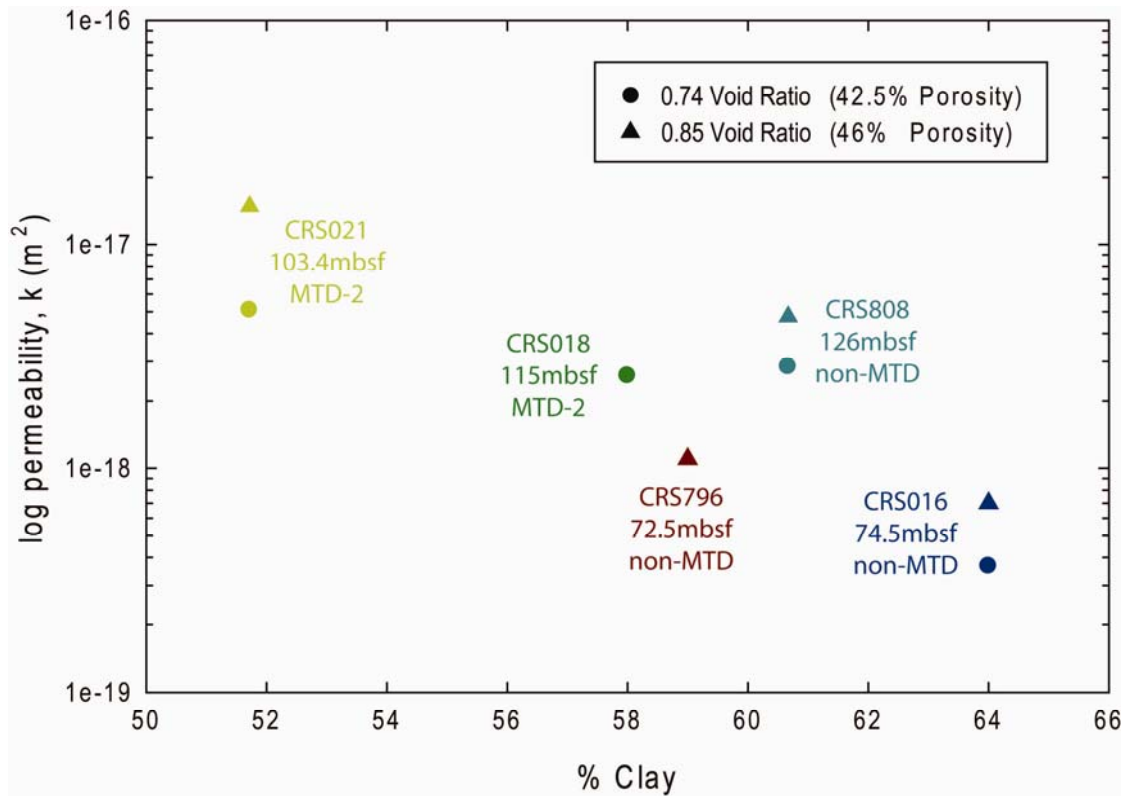


Figure 9: Ursa Grain Size versus Permeability

To best compare the effect of grain size on permeability, I took permeability calculations at the same porosity and plotted the results against % clay from grain size analysis (Table 3). Given the range of void ratios among the experiments, no one value encompassed all the experiments, so two void ratios were selected: 0.74 (circles) and 0.85 (triangles). The results indicate a general decrease in permeability with increase in clay content. This explains the higher permeability within the MTD-2 specimens.

with sufficient effective stress, the discrepancy in void ratio between MTD and non-MTD units becomes nonexistent, and the consolidation behaviors merge. Given a hydrostatic system and 3800kPa convergent effective stress, MTDs are indistinguishable from non-MTD units at 500mbsf (assuming 1.8g/cc). For Ursa overpressure conditions ( $\lambda^* = 0.6$ ), the depth to MTD erasure increases to 1250mbsf.

### **Synthetically Remolded Ursa Sediment**

To simulate the effect of debris flow shearing on the Ursa core specimens, I consolidated a remolded specimen (CRS021\_ut) from core U1322B 5H7 at 42mbsf. A previous Ursa study [Long, 2008] ran an experiment on an adjacent core, U1322D 1H2 from 42mbsf (CRS826\_mit). CRS826\_mit serves as a comparison of the intact material's response to consolidation. This shallow core is selected to simulate remolding along the depth of the plane of failure. It is important to note that these two cores are actually located within MTD-1, the less deformed MTD unit above MTD-2 (Figure 4). Thus the intact core already underwent debris-flow induced remolding.

### ***Remolded Ursa Results***

Synthetic remolding removes the specimens' pre-consolidation stress [Skempton, 1944; Leroueil *et al.*, 1985; Olson, 1986; Burland, 1990]. Consolidation of a remolded specimen ideally results in entirely plastic deformation, because the stress history is removed [Skempton, 1944; Leroueil *et al.*, 1985; Olson, 1986; Burland, 1990]. The ideal remolded consolidation curve will consist of a flat-sloped line of plastic deformation [Burland, 1990]. The transition of shallow to steep slope (Figure 10) in CRS021\_ut indicates initial elastic deformation. This may result from insufficient remolding, and thus preservation of stress history. The specimen was thoroughly kneaded by hand for 10 minutes (see Appendix A for full procedure).

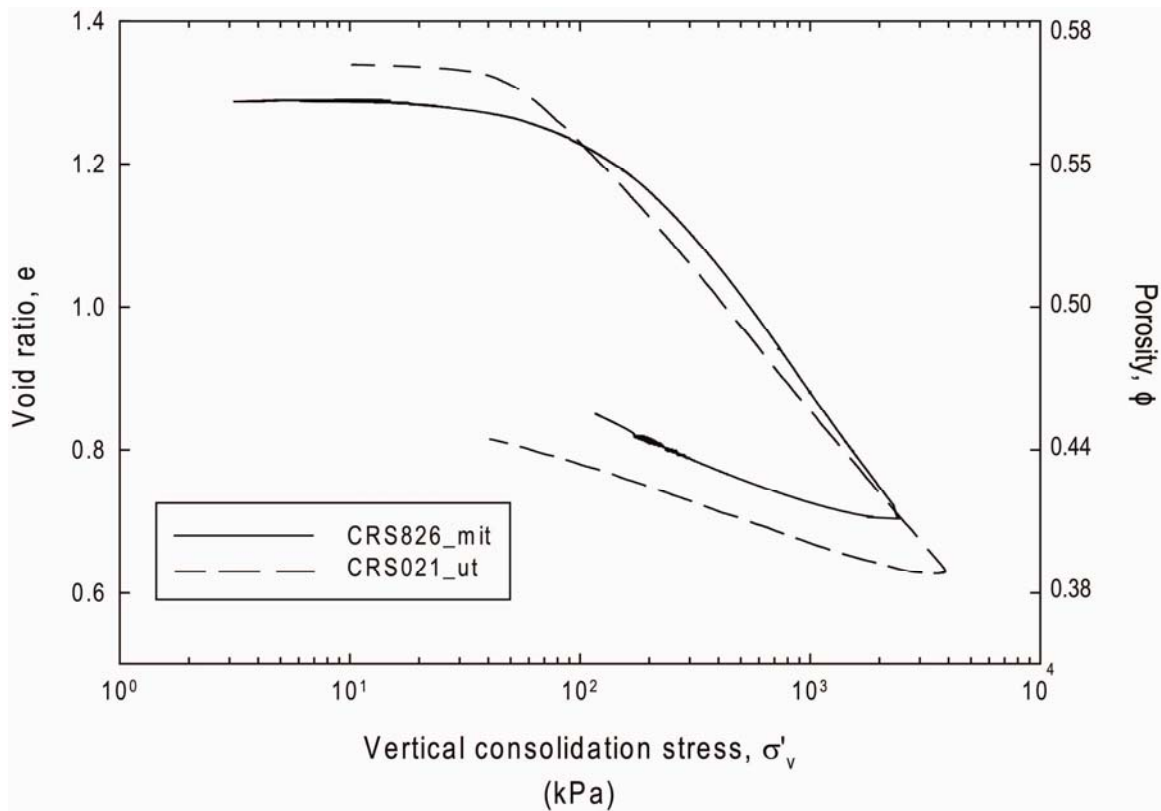


Figure 10: Ursa Intact and Remolded Consolidation Curves

Comparison of intact and remolded Ursa consolidation curves from 42mbsf. There is a slight leftward shift in the remolded curve, indicating this specimen has a lower void ratio for a given effective stress. However at stresses in excess 1000kPa, the curves appear to converge, as predicted by Skempton (1944). Table 4 summarizes data associated with these consolidation curves.

A slight leftward shift is apparent in the remolded curve; resulting in a lower void ratio at the same effective stress (Figure 10). The remolded curve also has a flatter slope, or lower compression index.  $C_c$  for the intact and remolded experiments are 0.4476 and 0.3839, respectively (Table 4). Despite the difference in compression indices, the expansion indices for both experiments are nearly identical;  $C_s$  for the intact sample is 0.0978, and 0.954 for remolded (Table 4). There is a notable convergence in the curves which I explore in the Discussion. It is also important to note that a slight change in void ratio of either specimen has strong control over the relative shift of the remolded curve. If the two initial void ratios were identical, a stronger leftward shift would be present.

The void ratio of CRS826\_mit, measured from moisture and density test, is 1.29 which corresponds to a porosity of 56% (Table 4). The remolded void ratio from CRS021\_ut is slightly higher at 1.34, corresponding to a porosity of 57% (Table 4). This could indicate some pore spaces were introduced into the material during remolding.

Permeability for the intact specimen, CRS826\_mit, at 56% in situ porosity is calculated as  $1.40\text{E-}17 \text{ m}^2$ . The remolded permeability is higher (Table 4); at an in situ porosity of 57%, the permeability is  $4.53\text{E-}16 \text{ m}^2$ . As with the intact Ursa experiments, permeability data are plotted over the normal consolidation curve,  $(k) = A\phi - B$  trend is fitted. The calculated trend for CRS021\_ut is  $\log(k) = 1.14\phi - 15.99$  (Table 4). I present two hypotheses for the increase in permeability of the remolded sample. (1) The remolding process altered the sediment fabric in a way that increases the ability of pore fluids to flow through the specimen during consolidation. (2) The insufficient amount of excess pore pressure generated during consolidation results in a falsely high permeability calculation. The first hypothesis is explored further in the Boston Blue Clay section and Discussion.

<b>Experiment</b>	<b>Depth (mbsf)</b>	<b>e</b>	<b><math>\Phi</math></b>	<b>P'c</b>	<b>Cc</b>	<b>Cs</b>	<b>Permeability log (k) (m<sup>2</sup>)</b>	<b>In Situ Perm (k) (m<sup>2</sup>)</b>
CRS021_ut	41.5	1.34	0.57	--	0.3792	0.1059	1.14x-15.99	6.67E-16
CRS826_ut	42	1.29	0.56	260	0.4550	0.1038	--	1.40E-17

Table 4: Intact and Remolded Ursa CRS Results

As with the intact experiments, void ratio and porosity are calculated from the specimen; P'c, Cc and Cs are interpreted from plots. In situ perm is calculated from the in situ porosity and permeability trend equation. The trend is calculated from permeability data in the virgin consolidation stage of the experiment.

The convergence of Cs curves may indicate that at some effective stress, the unique remolded and intact characteristics become indistinguishable. That is the deformation induced by vertical consolidation becomes greater than any shearing deformation induced by debris flow, and all specimens, regardless of geologic history, converge to one Ursa silty-clay consolidation behavior.

### **Resedimented Boston Blue Clay**

To explore the consolidation response of a clay specimen in its intact versus its remolded state, I conducted CRS tests on resedimented Boston Blue Clay (BBC). BBC is an illitic marine clay deposited within the Boston during glacial retreat [Kenney, 1964]. It is a well-studied material [Fayad, 1986; Santagata *et al.*, 2005; Sheahan and Watters, 1997].

Two experiments were run on intact specimens (CRS037\_ut and CRS039\_ut) and two experiments were run on remolded specimens (CRS038\_ut and CRS040\_ut) with remolded material derived from the cuttings of the intact specimens. To create a homogenous medium for controlled laboratory experiments, blocks of clay are excavated, dried, and then pulverized. The samples were then ‘resedimented’ in a procedure utilized by Mazzei [2008] and described in Appendix A. During resedimentation, each sample was loaded to 100kPa.

### ***Boston Blue Clay Results***

The intact samples have a higher saturation and higher water content than the remolded samples (Table 5). Water was likely lost in the remolding process. Drying of

<b>Experiment</b>	<b>Status</b>	<b>e</b>	<b><math>\Phi</math></b>	<b>% Water</b>	<b>P'<sub>c</sub></b>	<b>C<sub>c</sub></b>	<b>C<sub>s</sub></b>	<b>Permeability log (k) (m<sup>2</sup>)</b>	<b>In Situ Perm (k) (m<sup>2</sup>)</b>
CRS037_ut	resed	1.27	0.56	45.4	107	0.3474	0.0493	8.27x-20.71	8.51 E-17
CRS038_ut	remold	1.23	0.55	43.1	--	0.2359	0.0373	7.36x-20.54	2.44 E-17
CRS039_ut	resed	1.33	0.57	48.0	93	0.3455	0.0495	8.05x-20.53	1.14 E-16
CRS040_ut	remold	1.29	0.56	45.4	--	0.2325	0.0371	7.98x-20.98	4.20 E-17

Table 5: Resedimented and Remolded BBC CRS Results

As with the Ursa experiments, void ratio and porosity are calculated from the specimen; P'<sub>c</sub>, C<sub>c</sub> and C<sub>s</sub> are interpreted from plots. Water content is calculated from the specimen as the mass of water divided by mass of solids. In situ perm is calculated from the in situ porosity and permeability trend equation. The trend is calculated from permeability data in the virgin consolidation stage of the experiment.

the trimmings presumably occurred during intact sample preparation. Additional drying may have occurred when the material was molded into the confining ring. The initial void ratio of the intact samples is 1.30 and the remolded sample average is 1.26 (Table 5). This decrease in void ratio is not attributed to decrease in saturation, as that would actually increase the void ratio.

$$e = \frac{w_c * G_s}{S} \quad (4)$$

Therefore, the reduction in void ratio indicates the remolding process eliminated some pores (or pore space). The three dimensional nature of shearing clay is not entirely akin to uniaxial consolidation from the CRS experiments. Consolidation (loss of volume) is multi-dimensional in remolding, and one dimensional in CRS experiments.

The intact material (CRS037\_ut and CRS039\_ut) has a relatively stiff response (elastic deformation) from 0 to 100 kPa, the pre-consolidation stress or yield point. After 100kPa, the sample undergoes plastic deformation (Figure 11). As stated before, the slope of plastic deformation on a void ratio versus log effective stress curve defines the compression index ( $C_c$ ). The  $C_c$  values of the two intact samples, CRS037\_ut and CRS039\_ut, are 0.3474 and 0.3455, respectively (Table 5).  $C_e$  values, derived during unloading of the sample and representing the range of 3800kPa to 500kPa, are nearly identical at 0.0493 and 0.0495 (Table 5).  $P'_c$  for CRS037\_ut is 107kPa, and for CRS039\_ut is 93kPa. The slight offset in initial void ratio (1.27 vs. 1.33, Table 5) results in an offset in the intact compression curves.

The remolded curves, CRS038\_ut and CRS040\_ut, are also very similar. Both show primarily plastic deformation, as there is no clear break in slope (as is present in the intact curves) (Figure 11).  $C_c$  values for CRS038\_ut and CRS040\_ut are close at 0.2359



and 0.2325, respectively;  $C_e$  values are nearly identical at 0.0373 and 0.0371 (Table 5). The average initial void ratio of the remolded specimens is 1.26.

Comparison of the intact and the remolded BBC compression curves reveals a striking and consistent difference. Intact consolidation shows a distinct transition from elastic to plastic deformation at the laboratory-induced pre-consolidation stress of 100kPa. In contrast, the remolded compression curves show a linear decrease in void with increase in effective stress. The compression curves converge at the maximum consolidation stress, 3800kPa, at a void ratio of  $\sim 0.6$  (Figure 11).

The remolded specimens have much lower compression indices than the intact specimens (Table 5). This is due to the lack of elastic deformation in the initial consolidation stage within the remolded specimen (Figure 11). Plastic deformation begins at a much lower stress in the remolded specimen, than the intact specimen. The intact specimen withholds a greater amount of stress before abruptly consolidating. A good analogy is squeezing on styrofoam – the material initial resists until it abruptly crunches. The remolded specimens also have a lower swelling index (Table 5), indicating the effects of consolidation are better preserved, and the material will maintain a lower void ratio even when unloaded.

Permeability results (Figure 12) show distinct trends between the intact and remolded specimens. Using  $\log(k) = A\phi - B$ , the intact specimens (CRS037\_ut and CRS039\_ut) average  $\log(k) = 8.37\phi - 20.73$  (Figure 12). The remolded specimens (CRS038\_ut and CRS040\_ut) average  $\log(k) = 7.91\phi - 20.90$  (Figure 12). Thus, for a given void ratio, the permeability is higher within the intact specimens than in the remolded specimens.

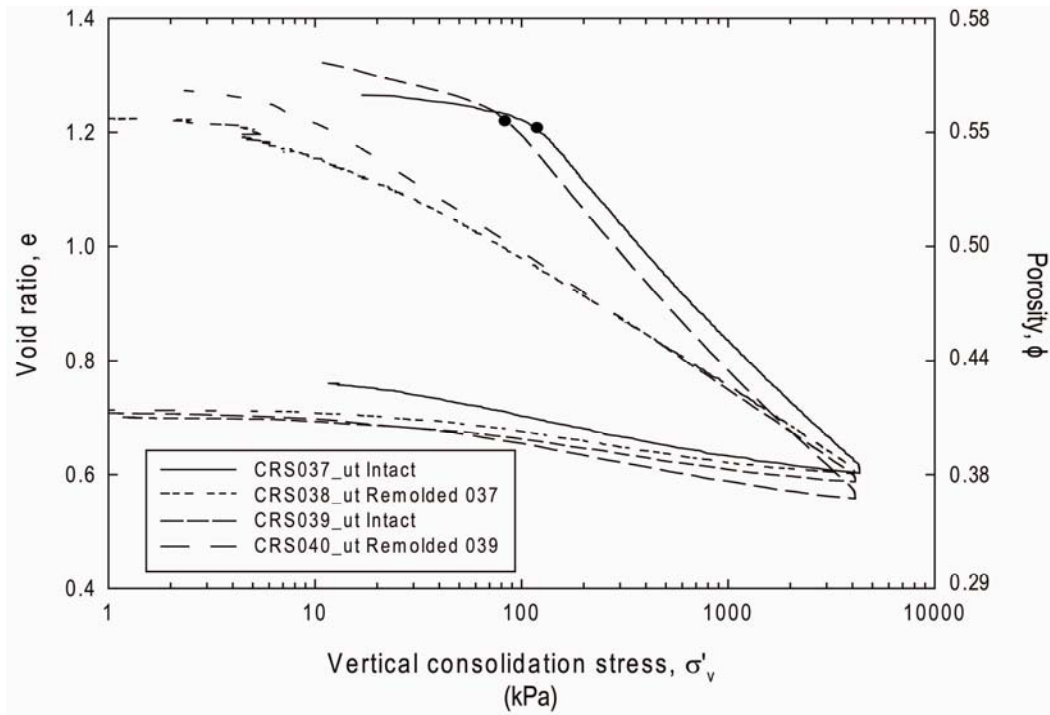


Figure 11: BBC Intact and Remolded Consolidation Curves

BBC consolidation curves show the same leftward shift in remolded specimens, with convergence of curves at the maximum consolidation stress, 3800kPa. The synthetic nature of this material shows the stark contrast in consolidation results of intact versus remolded. The remolded material has no initial, flat, elastic consolidation curve.  $P'_c$  interpretations are denoted as black circles. Table 5 summarizes data associated with these consolidation curves.

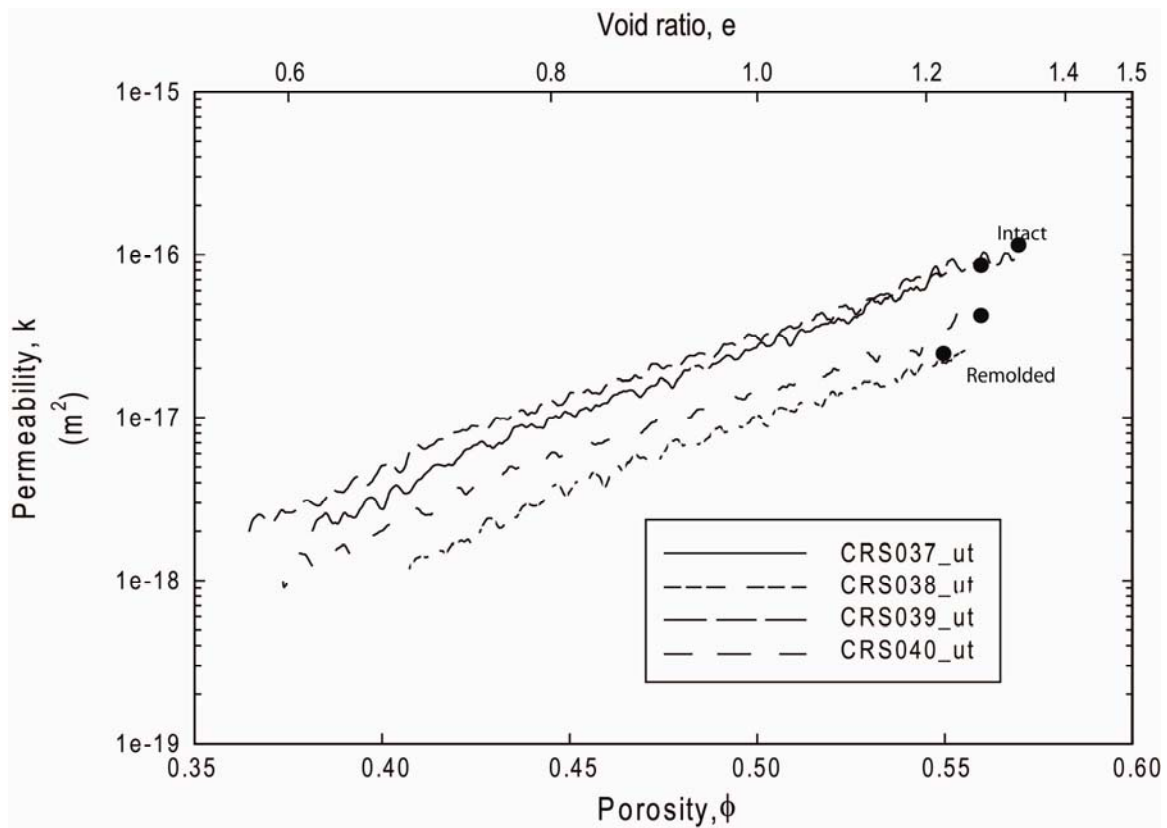


Figure 12: BBC Permeability

Permeability follows distinct intact and remolded trends. The intact samples, CRS037\_ut and CRS039\_ut, follow  $\log(k) = 8.37\phi - 20.73$ . The remolded samples, CRS038\_ut and CRS040\_ut, follow  $\log(k) = 7.91\phi - 20.90$ . The black circles correspond to calculated in situ permeability from the specimen-specific trends (Table 5).

## DISCUSSION

From seismic cross section, LWD data, and moisture and density calculations on CRS specimens, I interpret a sharp increase in density within the Mass Transport Deposits, relative to non-MTD sediments of similar lithology. In seismic (Figure 2) the density contrast is highlighted by the strong basal reflector separating MTD-2 from underlying non-MTD sediments. In LWD data (Figure 3), I observe a 5% decline in porosity across this same basal boundary of MTD-2. In CRS testing, void ratio measurements are lowest in the MTD-2 specimens, even compared to non-MTD sediments of greater depth (Figure 7).

One interpretation is the dense MTD units represent sediments at lower pore pressure (higher effective stress) than non-MTD sediments. Direct pore pressure measurements through the sediment column at Ursa during IODP Expedition 308 [Flemings *et al.*, 2008] refute this observation, recording a constant overpressure ratio of 60% in both MTD and non-MTD sediments. I confirm this pressure profile using the interpreted  $P'_c$  values from my experiments, and the previous study [Long, 2008], as proxy for in situ effective stress, calculating 57% average from MTD-2 and non-MTD sediments. The consistent trend in pressure profile at depth, irrespective of sedimentary unit indicates the consolidated MTD units reflect overall geologic loading conditions from sedimentation; and that MTDs do not represent a different pore pressure profile due to debris flow shearing or post-failure consolidation.

A second interpretation to explain the increase in density is that the shearing effect of slope failure altered the consolidation behavior of the sediment. Specifically, the MTD sediments have a new relationship in void ratio reduction at increasing effective stress. The consolidation experiments demonstrate a decline in the compression index of

both MTD and remolded specimens, compared to non-MTD and intact specimens (Figure 7). Previous studies show intact clay is much stronger and stiffer than remolded clay at the same void ratio. Goldschmidt first proposed in 1926 that remolding is akin to collapsing a “cardhouse” of clay particles [Mitchell, 1993], transitioning from random to parallel alignment. Lambe and Whitman (1969) show that for a thoroughly remolded soil, the effective stress is reduced as the load shifts from the grain structure to pore water. Remolding alters the sediment fabric by removing the pre-consolidation stress, thus weakening the MTD material and resulting in a greater consolidation of the remolded sediments at the same stress as non-MTD sediments.

I hypothesize MTD densification is a result of sediment remolding during debris flow. Several studies have made this assumption [Coleman and Prior, 1988; De Blasio, 2004; Gauer *et al.*, 2006; Pirmez *et al.*, 2004; Schwab *et al.*, 1996] particularly in modeling the Storegga Slide. The basal layer has the highest degree of shear and thus highest degree of remolding [Hampton, 1975]. Remolding reduces void space, eliminates pre-existing shear planes, destroys flocculated aggregates, and aligns grains along the preferred orientation of shear [Mitchell, 1993]. Casagrande [1932] proposed that marine sediments have a particular clay bond that is formed during flocculated deposition in salt, which is destroyed during remolding.

To determine how sediments react during consolidation, I ran CRS experiments on an MTD-2 and two non-MTD Ursa core specimens. The experiments (Figure 7) highlight a distinct difference in consolidation behavior between the two geologic units. The MTD specimens have much lower compression indices and in situ void ratios than non-MTD specimens, even those from a greater depth than MTD-2. However, the most significant observation is that while all of the specimens have different compression

indices and initial void ratios, the curves all converge to a common void ratio (0.55) at the maximum confining stress of the experiment (3800kPa).

To evaluate the hypothesis that MTDs represents remolded sediments, I conducted CRS consolidation experiments on remolded shallow Ursa core and compared the results to a previous experiment on an intact core of the same depth. Porosity at the base of MTD-is 5% less than non-MTD sediments immediately below, therefore a similar shift is expected in between the lab remolded and intact compression curves. Due to the 42mbsf core's location with MTD-1, a 5% shift in porosity is not expected. The specimen has already undergone a degree of remolding during debris flow, and is following an MTD consolidation path (Figure 13). Despite this, there is a slight leftward shift of the remolded curve (Figure 10).

However, at stresses greater than 1000kPa, the two consolidation curves converge, and continue this convergence in the unloading stage. The convergence of  $C_s$  curves may indicate that at some effective stress, the distinct consolidation characteristics of remolded and intact specimens become indistinguishable. Deformation induced by vertical consolidation becomes greater than any shearing deformation induced by debris flow. All specimens, regardless of geologic history, converge to one Ursa silty-clay consolidation behavior.

Due to the deformed nature of the intact sample, I ran an additional suite of intact and remolded consolidation experiments on synthetically resedimented Boston Blue Clay to examine the effect of remolding in ideal conditions. Burland [1990] conducted a thorough investigation on the consolidation behavior of several intact geologic specimens, laboratory resedimented specimens, and remolded specimens. Burland's [1990] results indicate a parallel shift in the field consolidation curve to the remolded curve, with no convergence expected. A previous study by Skempton [1944], however,

does show convergences in intact, remolded, and resedimented consolidation curves, particularly at effective stresses greater than 1000kPa. As both Figures 10 and 11 show, Ursa Clay and Boston Blue Clay in this study follow the convergence of Skempton [1944] not the parallel shift of Burland (1990).

All experiments of this study, MTD and non-MTD, intact and remolded, and resedimented and remolded, show a convergence of void ratio at the maximum effective consolidation stress (Figure 7, 10). This indicates that eventually the consolidation stress is significant enough to overcome the effect of remolding, essentially erasing MTDs by making the influence of overburden deformation greater than debris flow deformation. For Ursa and BBC experiments, this stress is approximately that of the confining stress, 3800 kPa, which corresponds to a hydrostatic depth of 500m, and an overpressured depth of 1250m for Ursa conditions.

From this study, the evolution of Ursa MTD's follows the steps illustrated in Figure 13. Initially, shallow Ursa sediments are consolidated uniaxially by progressive geologic loading (Figure 13, stage 1). At some point, slope failure triggers movement of the sediment down slope in form of a debris flow (Figure 13, stage 2). The shearing action of the debris flow weakens the sediment, reducing its ability to support the overburden. As consolidation resumes, the remolded sediment follows a new, less steep, curve. Within the geologic record, a distinctive dense, shallow unit provides evidence for historical slope failure. At a given effective stress, approximately 4000kPa, the remolded consolidation curve converges with the original intact curves at an approximate void ratio of 0.5 (Figure 13, stage 3). From this point, the consolidation behavior of the MTD is indistinguishable from surrounding non-MTD sediments.

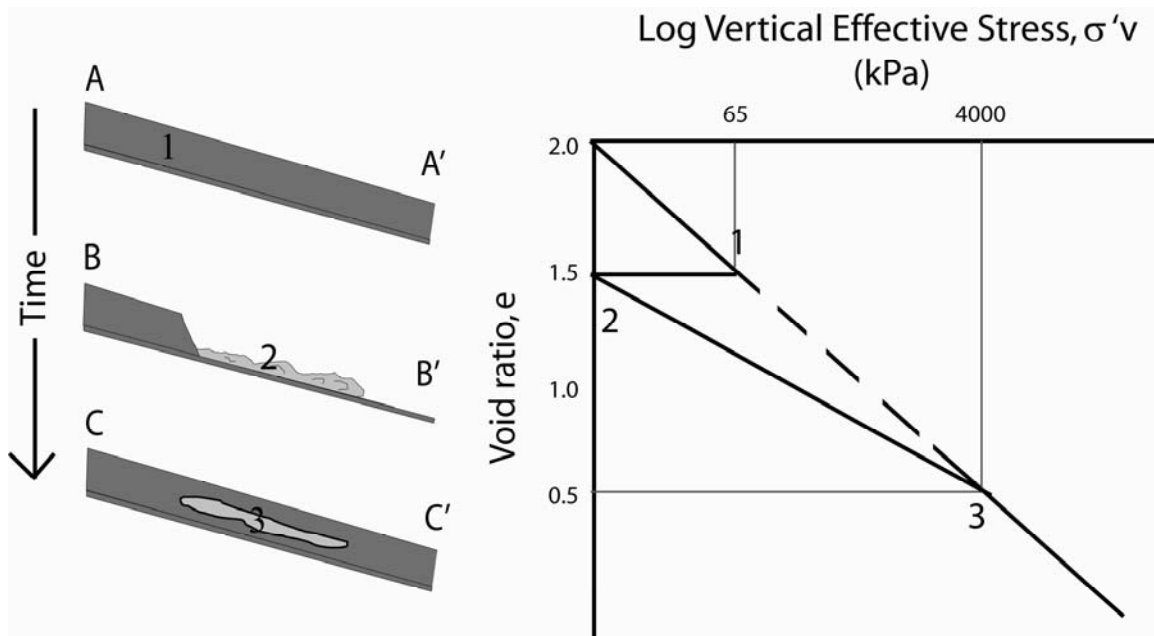


Figure 13: MTD Evolution

In stage 1, Ursa sediments were undergoing uniaxial consolidation from geologic loading. Given 0.6 overpressure ratio, the estimated effective stress at 30mbsf is 65kPa and estimated void ratio is 1.5. 30mbsf is the estimated depth of failure plane for MTD-2. In stage 2, debris flow occurs. Remolding preserves the in situ void ratio (1.5), however effective stress goes to 0. Consolidation resumes; however at a shallower slope (lower  $C_c$ ). In stage 3, the consolidation curve of the MTD approaches the non-MTD consolidation curve. From CRS experiments of this study, convergence occurs at approximately 4000kPa, at a void ratio of 0.5



## CONCLUSION

Analysis of seismic, core, logging, and consolidation data highlight the presence of ten prominent MTDs within the upper 200mbsf at drill site U1322 in Ursa Basin, indicating at least 10 major transport events occurred within the Late Pleistocene.

MTD units are identified:

- (1) In seismic as semi-transparent, chaotic units bounded by top and bottom reflectors
- (2) In LWD as zones of high resistivity and bulk density, and low porosity, in relation to surrounding undeformed units
- (3) In CT images as highly deformed cores with tilted bedding and low density zones evident of multiple thin fractures
- (4) In SEM images as sediments with clay particles wrapping around coarser quartz grains, closing off pore spaces, and forming a more aligned fabric
- (5) In CRS tests as specimens with low compression index and initial void ratio

Consolidation experiments on the non-MTD and MTD-2 specimens highlight key similarities and differences in these geologic units. The MTD-2 specimens have a lower void ratio at given effective stress, and lower compression index, than non-MTD sediments. However, the interpreted in situ effective stress of the specimens from Pre-consolidation stress indicate a consistent overpressure ratio of approximately 0.6 through the section. Permeability is slightly higher within MTD-2; however grain size analysis indicates this is likely due to a coarser grain composition within MTD-2 as compared to the non-MTD specimens. While the debris flow altered some properties of the MTD sediments, many properties of Ursa silty-clay are still preserved.

From consolidation experiments on both Ursa and BBC intact and remolded specimens, it is clear the MTD specimens do share characteristics with the remolded specimens. Despite the initial similarity in void ratio, the remolded specimens have a lower compression index than the intact specimens. These experiments add strength to my hypothesis that the shearing action of debris flow is akin to synthetic remolding. Remolding alters the sediment structure, and consolidation behavior, resulting in a lower void ratio at a given effective stress. This effect records the debris flow as a distinct, dense unit and explains why MTDs are recorded with a strong basal reflector in seismic data and as a high density zone in LWD data. Remolding also explains the unique consolidation behavior of the MTD versus non-MTD sediments. From these experiments, I have gained better insight into the geologic history of these dense sediments, post failure. I infer that as consolidation continues, like the experiments, the MTD and non-MTD sediments will converge to one compression curve at approximately 4000kPa.

Variable	Definition	Dimensions	SI Units
Cc	Compression index	Dimensionless	--
Ce	Expansion index	Dimensionless	--
Gs	Grain density	$M/L^3$	g/cc
K	Hydraulic conductivity	$L/T$	m/s
$P'_c$	Pre-consolidation stress	$M/LT^2$	kPa
SED	Strain energy density	$M/LT^2$	$KJ/m^3$
$C_v$	Coefficient of consolidation	$L^2/T$	$m^2/s$
e	Void ratio	Dimensionless	--
u	Pore pressure	$M/LT^2$	kPa
$u_b$	Back pressure	$M/LT^2$	kPa
$u_e$	Excess pore pressure	$M/LT^2$	kPa
$u_h$	Hydrostatic pore pressure	$M/LT^2$	kPa
w	Water content measured on trimmings	Dimensionless	--
$\rho_b$	Bulk density	$M/L^3$	g/cc
$\gamma_w$	Unit weight of water	$M/L^2T^2$	$kN/m^3$
$\sigma_v$	Vertical stress	$M/LT^2$	kPa
$\sigma'_v$	Vertical effective stress	$M/LT^2$	kPa
$\lambda^*$	Overpressure ratio	Dimensionless	--

Table 6: Nomenclature

## **APPENDIX A**

### ***Consolidation Experiments***

I conducted Constant Rate of Strain (CRS) Consolidation experiments on 4 specimens from site U1322 of the Ursa Basin, and 4 resedimented Boston Blue Clay (BBC) specimens. In this appendix I discuss the geologic history and significance of these two materials to this study. I then summarize results; review the sample preparation procedure, trimming, resedimenting and remolding techniques. I discuss the consolidation procedure as outlined in ASTM 4186. I also present a force-balance analysis of the CRS experiment. I conclude with tabulated results and figure plots. Nomenclature is defined in Table A1.

#### **URSA EXPERIMENTS**

I conducted Constant Rate of Strain (CRS) consolidation tests on 4 samples from Site U1322 at the University of Texas (UT) GeoMechanics laboratory to obtain consolidation properties of the soil and analyze the stress history in the upper 200mbsf of the Ursa Basin. The results are presented in Table A2.

#### **Ursa Summary**

Seismic, core and logging data indicate a series of MTDs at Ursa Basin. Studying the consolidation characteristics of MTD and non-MTD sediments provides insight into the origin and evolution of these failures. The transition from elastic to plastic deformation,  $P'_c$ , provides an estimate of maximum in situ effective stress [Becker, 1987; Casagrande, 1936]. Consolidation properties were determined from results of constant rate of strain consolidation (CRS) tests on intact samples.

The compression index ( $C_c$ ) refers to the slope of the normally consolidated portion of the compression curve in  $e$ -log ( $\sigma'_v$ ) space (Figures A3 – A10). The measured values of  $C_c$  range from 0.2217 to 0.5232.  $C_c$  decreases with void ratio. The expansion index ( $C_e$ ) refers to the slope of the unloading portion of the compression curve in the  $e$ -log ( $\sigma'_v$ ) space. It ranges from 0.0762 to 0.1682 and also decreases with void ratio. Expansion index is measured from the maximum stress, 3800kPa, to an unloading stress of 500kPa.

The in situ hydraulic conductivity ( $K_i$ ) is obtained by extrapolating the linear portion of the  $e$ -log ( $K$ ) relation to the in situ void ratio (Figures A3 – A10).. Values of  $K_i$  range from  $7.7 \times 10^{-11}$  to  $8.25 \times 10^{-9}$  m/s. The coefficient of consolidation,  $c_v$ , ranges from  $5.2 \times 10^{-8}$  and  $2.3 \times 10^{-7}$  m<sup>2</sup>/s.  $c_v$  increases with depth for the sediments

Pre-consolidation stress,  $P'_c$ , is determined using the work-stress method proposed by Becker et al., [Becker] (Figure A1).  $P'_c$  is significantly less than the hydrostatic vertical effective stress ( $\sigma'_{vh}$ ) at both Sites, and match with the 0.6 measured overpressure ratio at Ursa.

## **BOSTON BLUE CLAY EXPERIMENTS**

I conducted CRS tests on two intact and two remolded Boston Blue Clay specimens at the University of Texas (UT) GeoMechanics laboratory to compare the consolidation curves and other properties of the deformed specimens. Remolding simulates debris flow shearing, and these tests serve as a proxy for the change in consolidation characteristics post slope failure. The compression index ( $C_c$ ) averages 0.3465 for intact samples and 0.2342 for remolded samples. The expansion index ( $C_e$ ) averages 0.0494 for intact samples and 0.0371 for remolded samples. The in situ hydraulic conductivity ( $K_i$ ) averages  $1.06 \times 10^{-18}$  m/s for intact samples and  $2.50 \times 10^{-17}$

m/s for remolded samples. The coefficient of consolidation ( $c_v$ ) averages  $1.70\text{E-}7 \text{ m}^2/\text{s}$  for intact samples and  $1.15\text{E-}7 \text{ m}^2/\text{s}$  for remolded samples.

### **Boston Blue Clay Summary**

Boston Blue Clay is an extensively studied sediment whose consolidation properties are well documented. I used this material to study the change in  $C_c$ ,  $C_e$ ,  $K$  and  $C_v$  when an intact sample is remolded in the laboratory. The compression index ( $C_c$ ) averages 0.3465 for intact samples and 0.2342 for remolded samples (Table A2). The expansion index ( $C_e$ ) is measured for an OCR of 5 and averages 0.0494 for intact samples and 0.0371 for remolded samples. The in situ hydraulic conductivity ( $K_i$ ) averages  $1.06 \times 10^{-18} \text{ m/s}$  for intact samples and  $2.50 \times 10^{-17} \text{ m/s}$  for remolded samples. The coefficient of consolidation ( $c_v$ ) averages  $1.7\text{E-}7 \text{ m}^2/\text{s}$  for intact samples and  $1.15\text{E-}7 \text{ m}^2/\text{s}$  for remolded samples.

Pre-consolidation stress,  $P'_c$ , is determined using the work-stress method (Figure A1) proposed by [Becker]. The resedimentation method gives a known pre-consolidation stress of 100kPa; therefore it is expected that all the intact samples have a  $P'_c$  of 100kPa. CRS037\_ut has a  $P'_c$  of 110kPa and CRS039\_ut has a  $P'_c$  of 90kPa, the average is the expected value of 100kPa (Table A2).

## **LABORATORY TESTING METHODOLOGY**

### **Ursa Sample Handling and Preparation**

Whole core samples were capped and sealed in wax onboard the drilling ship to preserve in situ saturation. All cores are stored in a refrigeration unit at the University of Texas at Austin. Specimens are removed in 2" sections from the core using a band saw. The core section is extruded and trimmed into a confining ring 5.0cm in diameter and 1"

in height. A recess tool sets the specimen height at 0.94” allowing the porous stone to sit within the top of the confining ring.

### **BBC Reconstitution and Preparation**

The BBC specimens are reconstituted from dried pulverized clay-sized grains mixed 1:1 with salt water (16 grams NaCl per liter) and vacuum deaired. The first four masses, 60g, 120g, 250g, and 1000g are added in 24-hour increments. Additional loads, 2000g, 4000g, 8000g, 10000g, and 12000g, are added as the specimen reaches the end of primary consolidation for each prior load (determined using a linear displacement transducer) [Mazzei, 2008]. The total load is equivalent to 100kPa. The resedimented specimen core is extruded and trimmed into a confining ring 5.0cm in diameter and 1” in height. A recess tool sets the specimen height at 0.94” allowing the porous stone to sit within the top of the confining ring.

### **Remolding Technique**

The remolding process for Ursa and BBC material are very similar. To remold the Ursa material, I placed 14 cubic inches of core material into a food storage bag, then used a standard food sealer to apply a vacuum for 15 seconds, removing air from the bag. I kneaded the bag for 10 minutes, thoroughly remolding the material. For BBC experiments, trimmings from the intact specimen are saved to create the remolded specimen; as indicated in Table 3, CRS038\_ut is remolded CRS037\_ut material, and CRS040\_ut is remolded CRS039\_ut material. For both Ursa and BBC, the material is then hand molded into a 5.0cm-diameter confining ring through smearing small quantities of the specimen into the ring at a time, preventing any large voids from forming. For BBC I squished the trimmings in my hand before smearing the material in to remold the material.

## Water Content

Two water contents were measured in the consolidation test:  $w_c$  and  $w_n$ .  $w_c$  is the water content measured on the trimmings during sample preparation.  $w_n$  is the water content measured on the test specimen itself. Water content is calculated by oven-drying the samples, then taking the difference in the weight of a soil before and after oven-drying, and dividing this difference by the oven-dried weight. Results are in Table A2.

## CONSTANT RATE OF STRAIN EXPERIMENTS

The CRS tests were conducted in the UT GeoMechanics laboratory per ASTM D4186 [International, 2003]. Specimen dimensions are 5.0cm in diameter and 2.39cm in height. Specimens were laterally confined with a steel ring. Prior to testing, specimens were saturated with de-ionized water and backpressured to 386 kPa for 24 hours to drive any gases present into solution. I applied a constant rate of strain using a computer-controlled load frame, with the sample base undrained and the sample top open to the backpressure. I continuously monitored sample height ( $H$ , in mm), applied vertical stress ( $\sigma_v$ , in kPa), and basal pore pressure ( $u$ , in kPa).

The vertical effective stress ( $\sigma'_v$ ), hydraulic conductivity ( $K$ ), compressibility ( $m_v$ ), coefficient of consolidation ( $c_v$ ) and strain energy density (SED) were calculated using the following equations [Tan, 2006]:

$$\sigma'_v = \sigma_v - \frac{2}{3} \cdot \Delta u \quad (1)$$

$$K = \frac{\dot{\varepsilon} \cdot H_0 \cdot H \cdot \gamma_w}{2 \cdot \Delta u} \quad (2)$$

$$m_v = \frac{\Delta \varepsilon}{\Delta \sigma'_v} \quad (3)$$



$$c_v = \frac{K}{m_v \cdot \gamma_w} \quad (4)$$

$$SED = \frac{\sigma'_{vi-1} + \sigma'_{vi}}{2} \cdot \ln\left(\frac{1 - \varepsilon_{i-1}}{1 - \varepsilon_i}\right) \quad (5)$$

All variables are presented in Table 2.

### Force Balance

While the load cell applies a measured force ( $F_d$ ) down on the specimen area ( $A$ ), this is not the true force the specimen experiences. The effective weight of the piston ( $W_p$ ) adds a downward force, and the cell pressure ( $u_c$ ) pushing up on the effective area ( $a$ ) of the piston adds an upward force (Figure A02). The piston weight and area are calculated using results of the uplift test. Using a force balance approach, the net load ( $F_{true}$ ) is calculated as follows:

$$F_{true} = F + W_p + u_c \cdot A - u_c \cdot a$$

The total stress ( $\sigma_v$ ) acting over the area of the specimen is:

$$\sigma_v = F_{true} / A = (F + W_p + u_c \cdot A - u_c \cdot a) / A$$

$$\sigma_v = u_c + (F + W_p - u_c \cdot a) / A$$

The effective stress ( $\sigma_v'$ ) is:

$$\sigma_v' = \sigma_v - [(2/3) \cdot (u_p - u_c)] - u_c$$

Where is ( $u_c$ ) pore pressure.

### LABORATORY TESTING RESULTS

Table 3 gives a summary of the details of each CRS test. Figures A3 to A10 show the consolidation curves in both  $e$ -log ( $\sigma_v'$ ) and  $\varepsilon$ -log ( $\sigma_v'$ ), normalized excess pore pressure, coefficient of consolidation ( $c_v$ ), strain energy density, and hydraulic

conductivity ( $K$ ) for each CRS test. Table 4 also summarizes details of previous CRS tests run on Ursa core material that is referenced in the main paper. The CRS data sheet can be found online in excel format under the “**Supplementary material**” section.

Variable	Definition	Dimensions	SI Units
Cc	Compression index	Dimensionless	--
Ce	Expansion index	Dimensionless	--
Gs	Grain density	$M/L^3$	g/cc
H	Height of specimen	L	mm
H <sub>0</sub>	Initial height of specimen	L	mm
K	Hydraulic conductivity	L/T	m/s
K <sub>i</sub>	In-situ hydraulic conductivity	L/T	m/s
OCR	Over consolidation ratio	Dimensionless	--
P' <sub>c</sub>	Pre-consolidation pressure	$M/LT^2$	kPa
SED	Strain energy density	$M/LT^2$	KJ/m <sup>3</sup>
S <sub>i</sub>	Initial saturation	Dimensionless	--
c <sub>v</sub>	Coefficient of consolidation	$L^2/T$	m <sup>2</sup> /s
e	Void ratio	Dimensionless	--
e <sub>i</sub>	Initial void ratio measured on specimen	Dimensionless	--
k <sub>i</sub>	In-situ permeability	L <sup>2</sup>	m <sup>2</sup>
m <sub>v</sub>	Frame compressibility	$LT^2/M$	1/kPa
u	Basal pore pressure	$M/LT^2$	kPa
u <sub>b</sub>	Back pressure	$M/LT^2$	kPa
w <sub>c</sub>	Water content measured on trimmings	Dimensionless	--
w <sub>n</sub>	Water content measured on specimen	Dimensionless	--
Δu	Excess pore pressure	$M/LT^2$	kPa
Δu/σ <sub>v</sub>	Normalized excess pore pressure	Dimensionless	--
δε/δt	Strain rate	1/T	%/hr
ε	Axial strain	Dimensionless	%
ε <sub>i</sub>	Axial strain prior to compression	Dimensionless	%
ρ <sub>b</sub>	Bulk density	$M/L^3$	g/cc
γ <sub>w</sub>	Unit weight of water	$M/L^2T^2$	kN/m <sup>3</sup>
σ <sub>v</sub>	Applied vertical stress	$M/LT^2$	kPa
σ' <sub>v</sub>	Vertical effective stress	$M/LT^2$	kPa
σ' <sub>iv</sub>	Vertical effective stress prior to compression	$M/LT^2$	kPa
σ' <sub>vh</sub>	Hydrostatic vertical effective stress	$M/LT^2$	kPa
σ' <sub>vm</sub>	Maximum vertical effective stress during consolidation	$M/LT^2$	kPa

Table A1: Appendix Nomenclature

Spec. Location		Index Test	Specimen Data		Test Conditions		Consolidation	
Test #	Depth	$w_c$	$w_n$	$e_i$	$u_b$	$\varepsilon_i$ (%)	$C_c$	$c_v$ (m <sup>2</sup> /s)
Hole	Location	SD		$S_i$ (%)	$\sigma'_{iv}$	$\delta\varepsilon/\delta t$ (%/hr)	$C_e$	$K_i$ (m/s)
Core-section		# obs		$G_s$		$\Delta u/\sigma_v$ @ $\sigma'_{vm}$ (%)	$P'_c$ (kPa)	$k_i$ (m <sup>2</sup> )
CRS016	74.5	41.1	44.0	1.24	386	0.07	0.5223	6.4E-8
1322D	75.43	1.6		99.4	4	0.5	0.1682	6.95E-11
2H-4WR		4		2.74		5.8	230	6.32E-18
CRS017	125.8	35.0	37.1	1.04	386	0.08	0.3792	2.3E-7
1322B	126.09	1.7		99.4	19	0.5	0.1059	9.10E-9
15H-1WR	100-125	4		2.74		0.7	330	8.27E-16
CRS018	114.56	27.7	27.3	0.82	386	0.09	0.2217	3.3E-8
1322B	114.56	0.7		92.6	19	0.6	0.0762	4.53E-11
13H-6WR		4		2.74		3.0	275	4.11E-18
CRS021	42.0	44.9	45.1	1.34	386	-0.4	0.3792	6.4E-6
1322B	42.49	0.8		99.3	12	0.8	0.1059	7.34E-9
5H-7WR		3		2.74		0.0	Remold	6.67E-16
CRS037	--	--	45.4	1.27	386	0.08	0.3474	1.7E-7
BBC	--	--		99.8	12	1.2	0.0493	9.36E-10
	--	--		2.78		1.6	107	8.51E-17
CRS038	Sourced	--	43.1	1.23	386	0.01	0.2359	1.2E-7
BCC	From	--		97.7	45	1.0	0.0373	2.68E-10
Remolded	CRS037	--		2.78		2.6	Remold	2.44E-17
CRS039	--	--	48.0	1.33	386	0.03	0.3455	1.7E-7
BBC	--	--		100.1	6	1.2	0.0495	1.25E-09
	--	--		2.78		1.8	80	1.14E-16
CRS040	Sourced	--	45.4	1.29	386	0.006	0.2325	1.1E-7
BBC	From	--		97.9	1	0.9	0.0371	4.62E-10
remolded	CRS039	--		2.78		2.0	Remold	4.20E-17

Table A2. UT CRS Test Conditions and Consolidation Properties

Notes: 1) See Table 2 for variables that were used in headings. 2) In column 2, "Depth" in the first row gives depth of the top of the whole core sample in mbsf (see Table 1, column 2). "Location" provides the specimen location in meters relative to the top of the whole core sample. "Depth" in the third row provides depth of the tested specimen in mbsf. 3) In column 3, "# obs" refers to the numbers of measurements; "SD" refers to the standard deviation. 4)  $e_i$  is calculated from  $w_c$  assuming a grain density of 2.74 and accounts for salt in the pore fluid settling out into a solid after the specimen is dried.

Spec. Location		Index Test	Specimen Data		Test Conditions		Consolidation	
Test #	Depth	$w_c$	$w_n$	$e_i$	$u_b$	$\varepsilon_i$ (%)	$C_c$	$c_v$ (m <sup>2</sup> /s)
Hole	Location	SD		$S_i$ (%)	$\sigma'_{iv}$	$\delta\varepsilon/\delta t$ (%/hr)	$C_e$	$K_i$ (m/s)
Core-section		# obs	$\rho_b$	$G_s$		$\Delta u/\sigma_v$ @ $\sigma'_{vm}$ (%)	$P'_c$ (kPa)	$k_i$ (m <sup>2</sup> )
CRS826	42	44.6	45.21	1.29	387	0.05	0.455	2.00E-8
1322D	42.87	1.8		97.4	5	0.21	0.1038	1.40E-17
1H2		3	1.763	2.78		7.5	260	1.40E-17
CRS796	72	46.3	47.25	1.281	384	0.05	0.4675	1.7E-8
1322D	72.78	0.8		102.6	2	0.25	0.1114	1.46E-10
2H2		2	1.795	2.78		13.5	280	1.46E-17
CRS021	103.4	31.7	32.91	0.916	387	0.00	0.2749	5.2E-8
1322D	103.44	1.0		97.03	15	0.30	0.0727	2.27E-10
3H3		4	1.873	2.7		4.52	274	2.27E-17
CRS808	125.8	34.1	37.39	1.080	396	-0.07	0.3123	8.0E-8
1322B	126.28	1.2		96.3	5	0.20	0.0500	2.44E-10
15H1		2	1.837	2.78		1.7	516	2.44E-17

Table A3. Previous Ursa CRS Test Conditions and Consolidation Properties

Notes: 1) See Table 2 for variables that were used in headings. 2) In column 2, “Depth” in the first row gives depth of the top of the whole core sample in mbsf (see Table 1, column 2). “Location” provides the specimen location in meters relative to the top of the whole core sample. “Depth” in the third row provides depth of the tested specimen in mbsf. 3) In column 3, “# obs” refers to the numbers of measurements; “SD” refers to the standard deviation. 4)  $e_i$  is calculated from  $w_c$  assuming a grain density of 2.74 accounts for salt in the pore fluid settling out into a solid after the specimen is dried. [Long *et al.*, 2008]

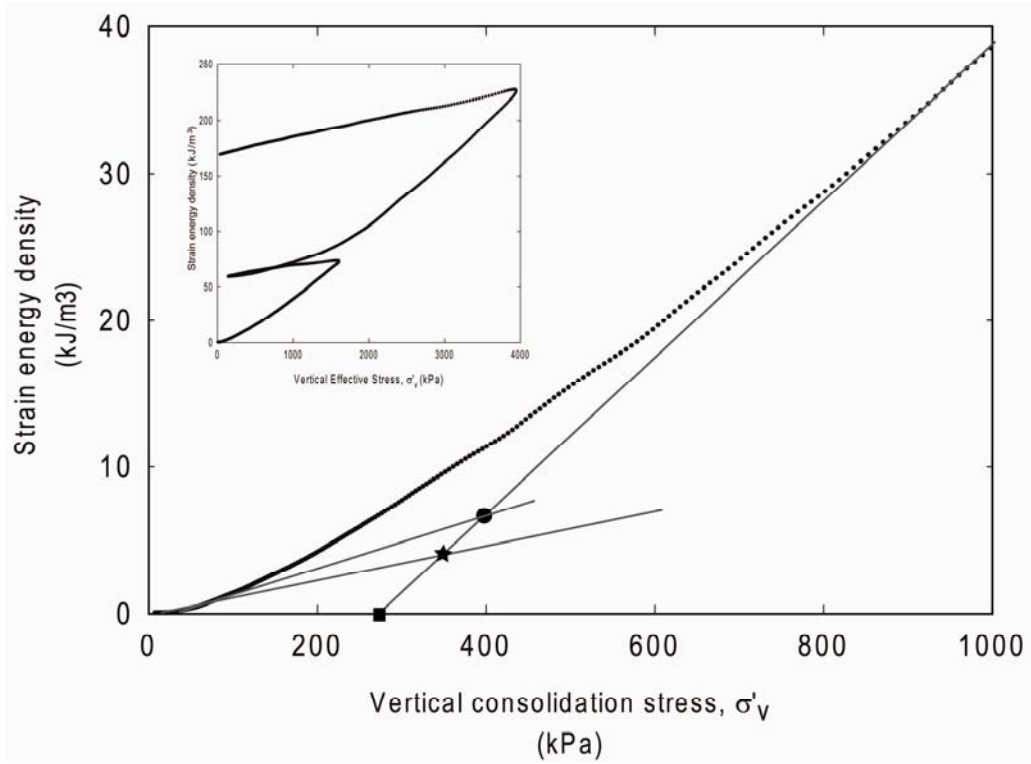


Figure A1: Pre-Consolidation Stress Interpretation Method

Strain energy density method of interpreting Pre-consolidation stress from Becker et al 1987. The intersection of the two slopes is  $P'_c$  (Star). Minimum  $P'_c$  is interpreted as the intersection of the slope of the virgin consolidation curve with the x-axis (Square). Maximum  $P'_c$  is interpreted by taking the intersection of steepest slope of the initial loading curve with the virgin curve (Circle).

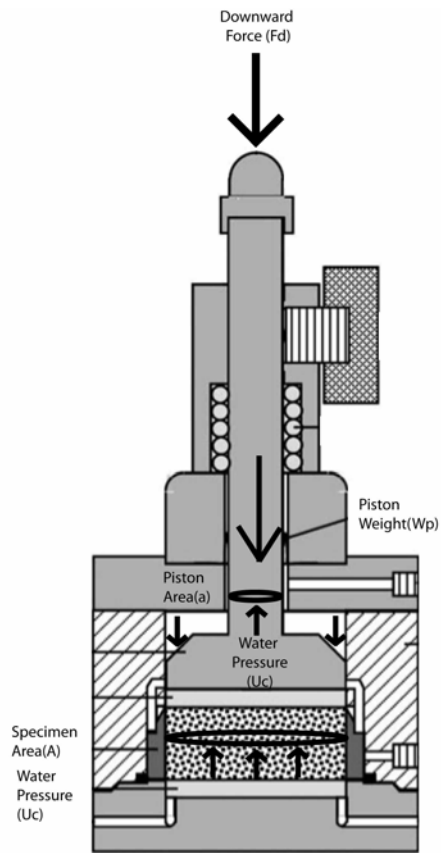


Figure A2: Force Balance Analysis of Consolidation Experiments.

Downward forces acting on the specimen are the downward force ( $F_d$ ) of the load cell and weight of the piston ( $W_p$ ). Water pressure in the cell provides an upward force over the area of the sediment ( $U_c \cdot A$ ), and a downward force over the area of the sediment ( $U_c \cdot A$ ), less the area of the piston ( $U_c \cdot a$ ).

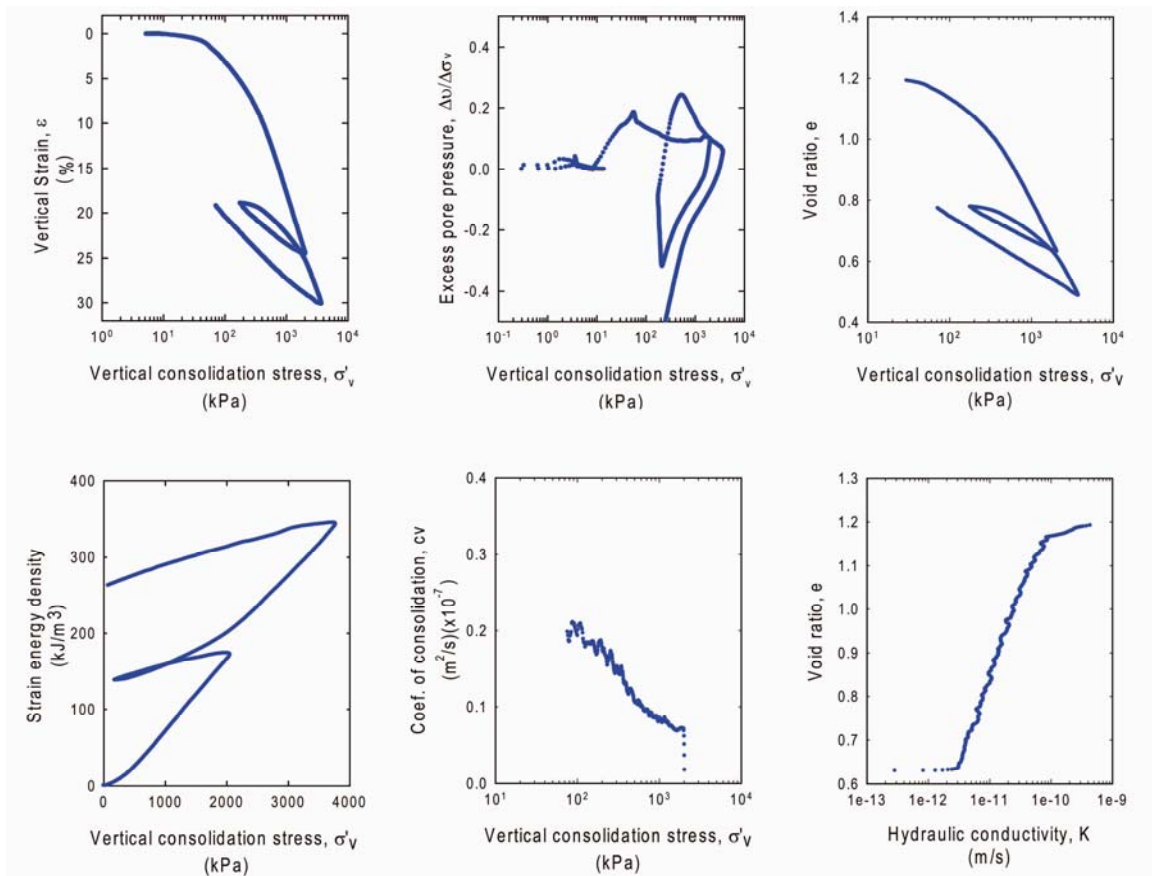


Figure A3: CRS016\_ut Consolidation Data

Sample 308-U1322D-2H-4WR, 74.5 mbsf



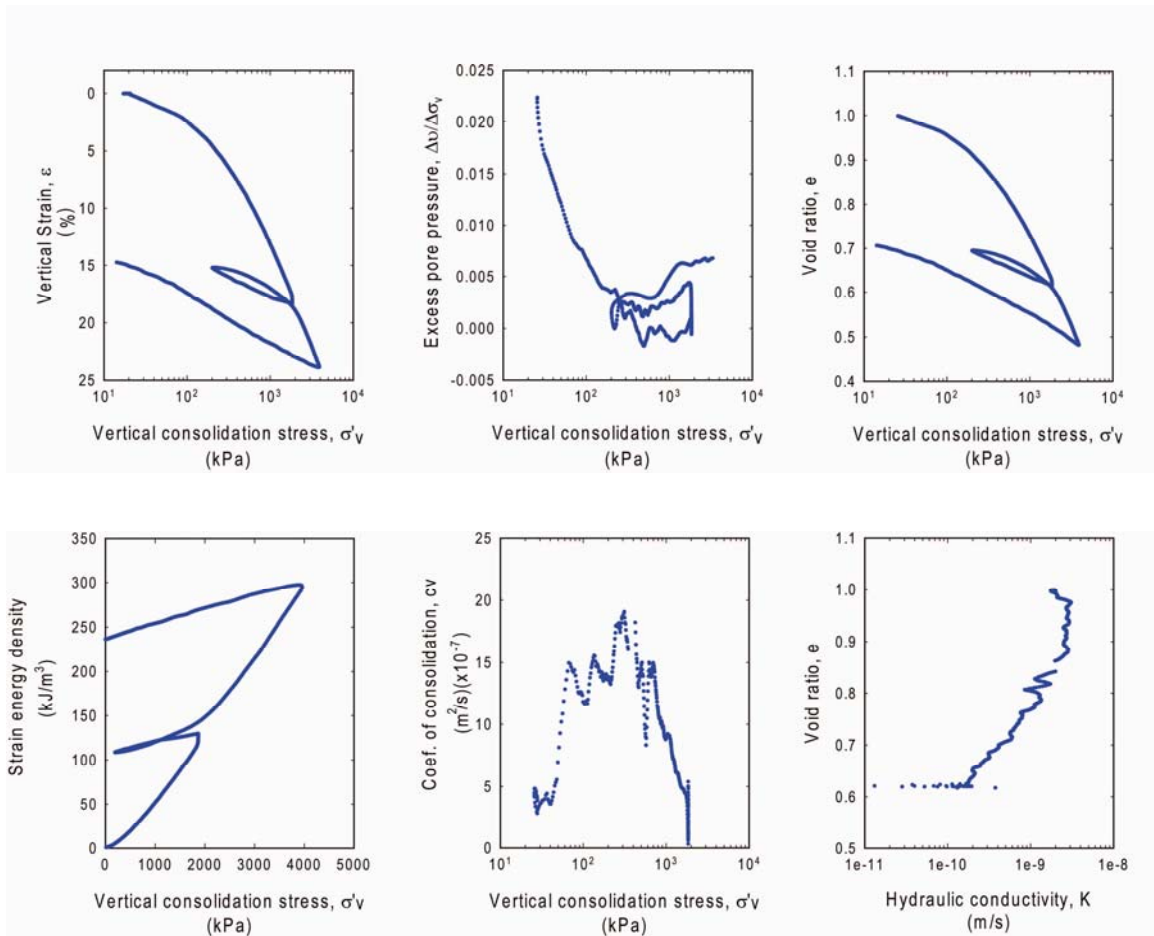


Figure A4: CRS017\_ut Consolidation Data

Sample 308-U1322B-15H-1WR, 125.8 mbsf

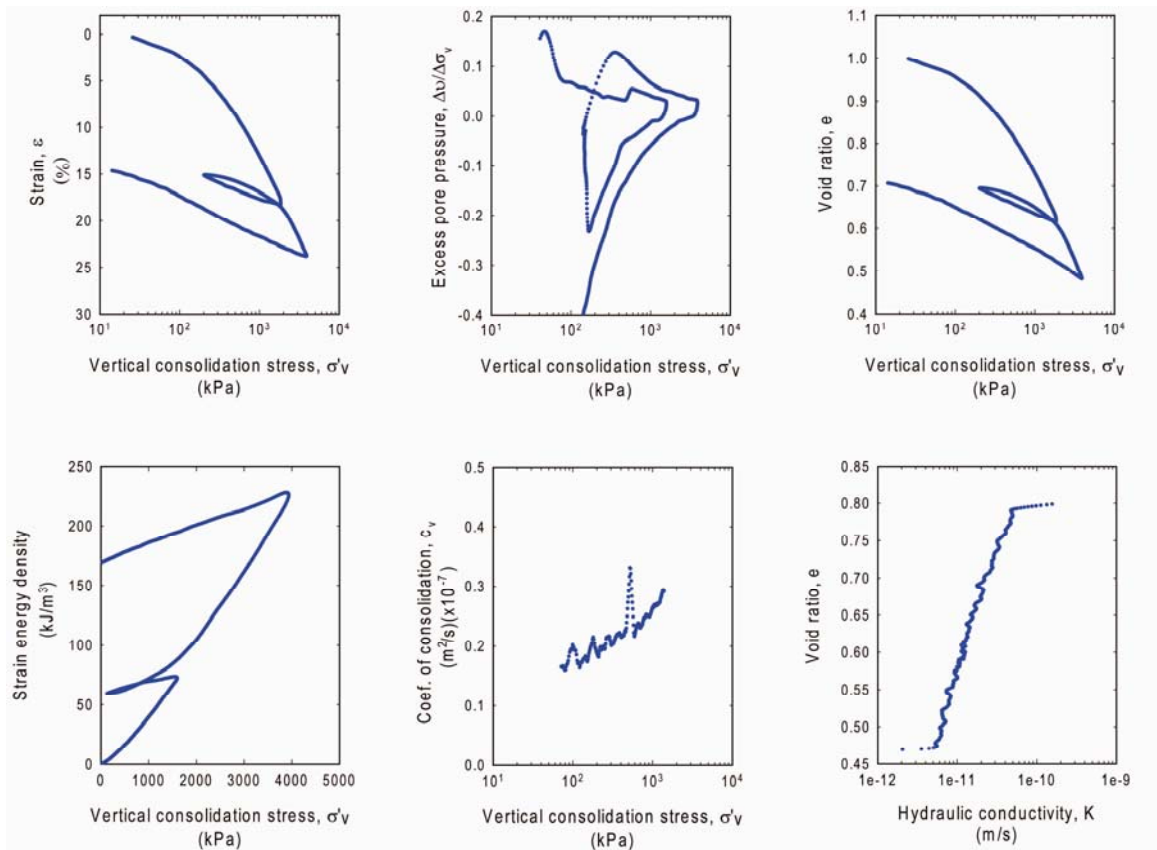


Figure A5: CRS018\_ut Consolidation Data

Sample 308-U1322B-13H-6WR, 114.6 mbsf

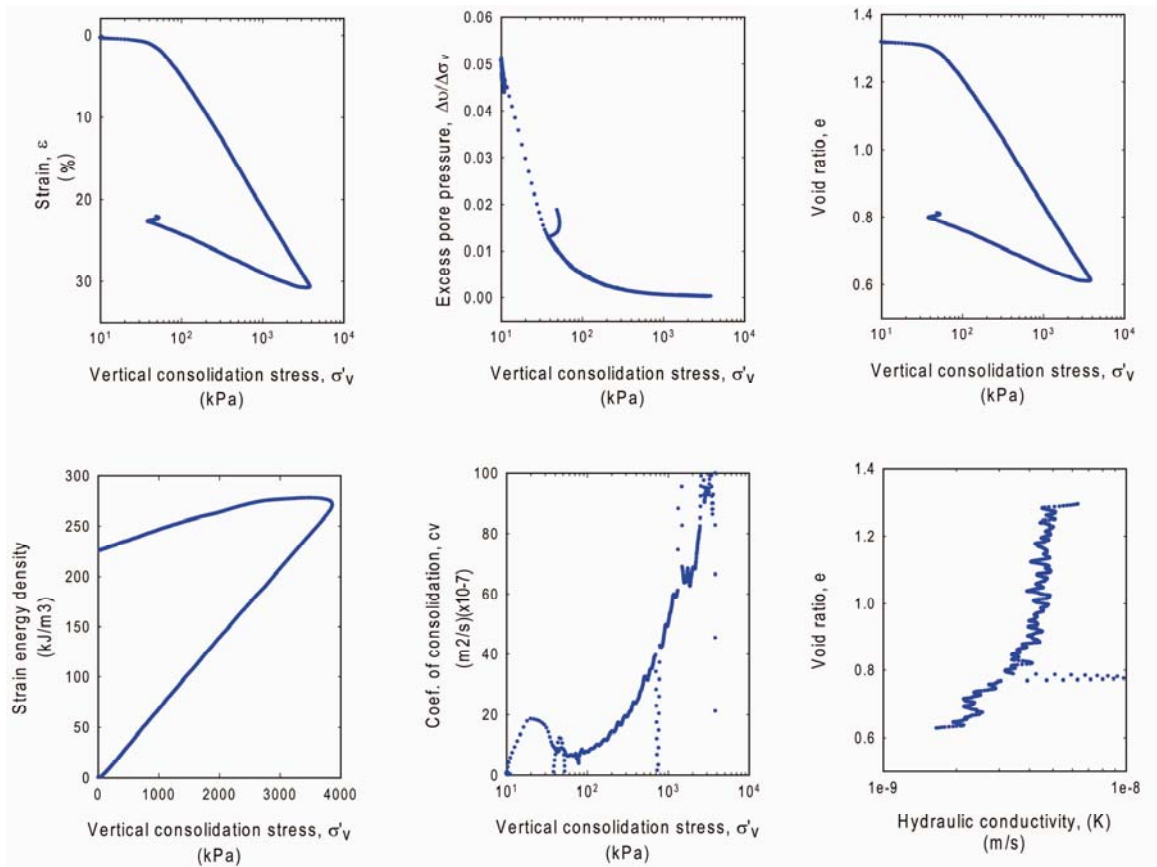


Figure A6: CRS021\_ut Consolidation Data

Sample 308-U1322D-5H-7WR, 42 mbsf

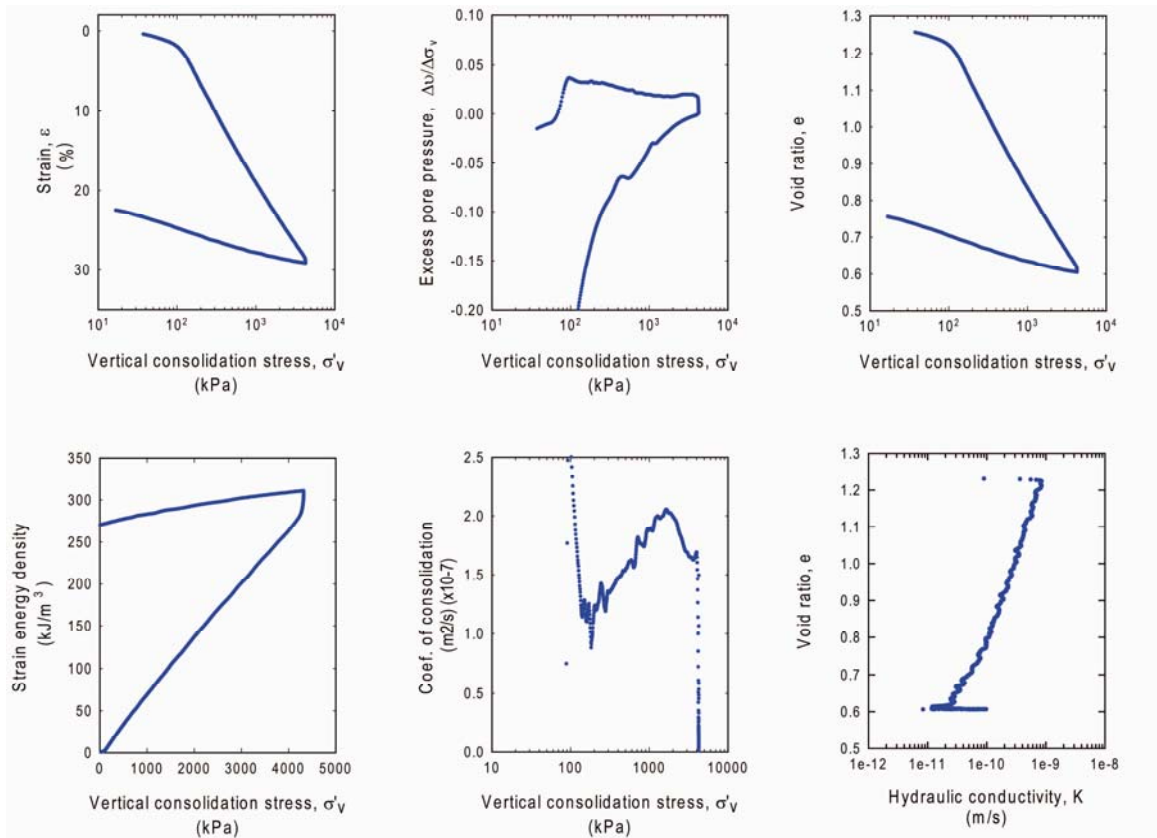


Figure A7: CRS037\_ut Consolidation Data

Intact Boston Blue Clay

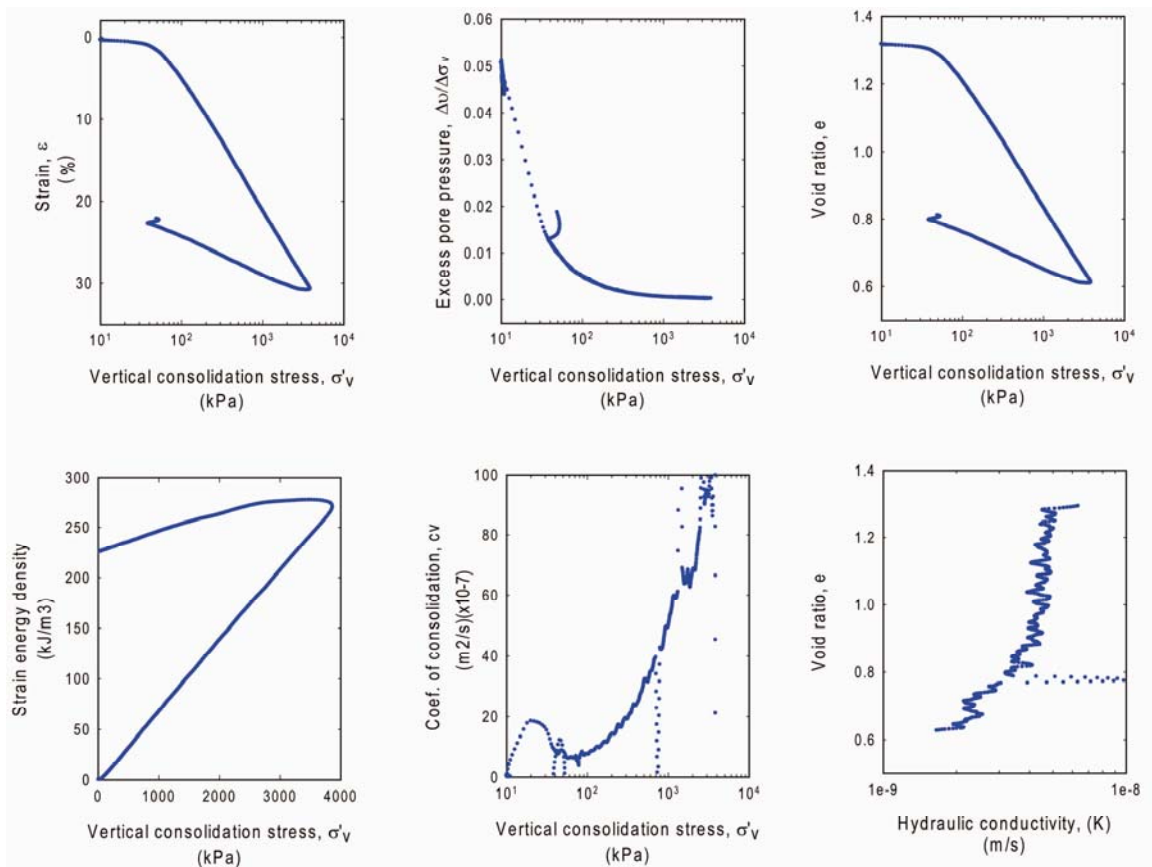


Figure A8: CRS038\_ut Consolidation Data

Remolded Boston Blue Clay from CRS037\_ut trimmings

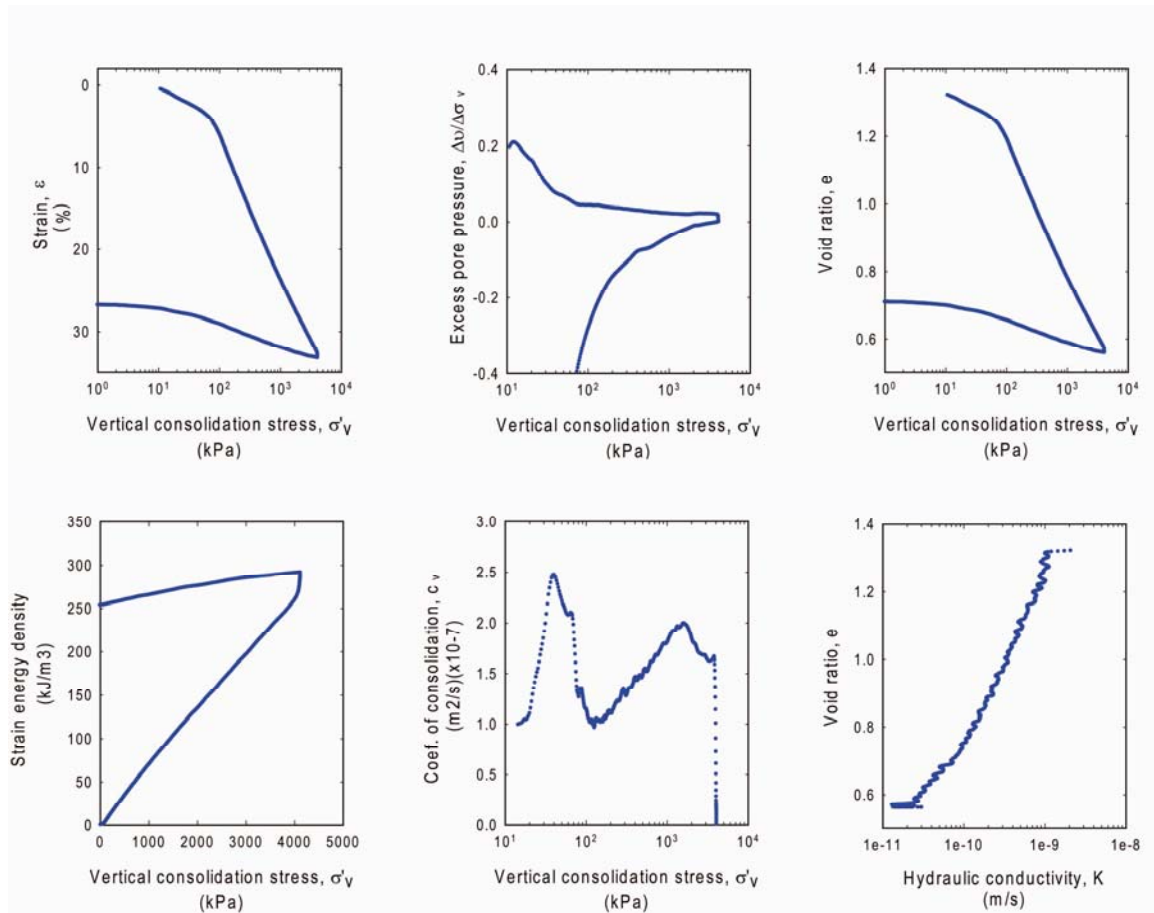


Figure A9: CRS039\_ut Consolidation Data

Intact Boston Blue Clay

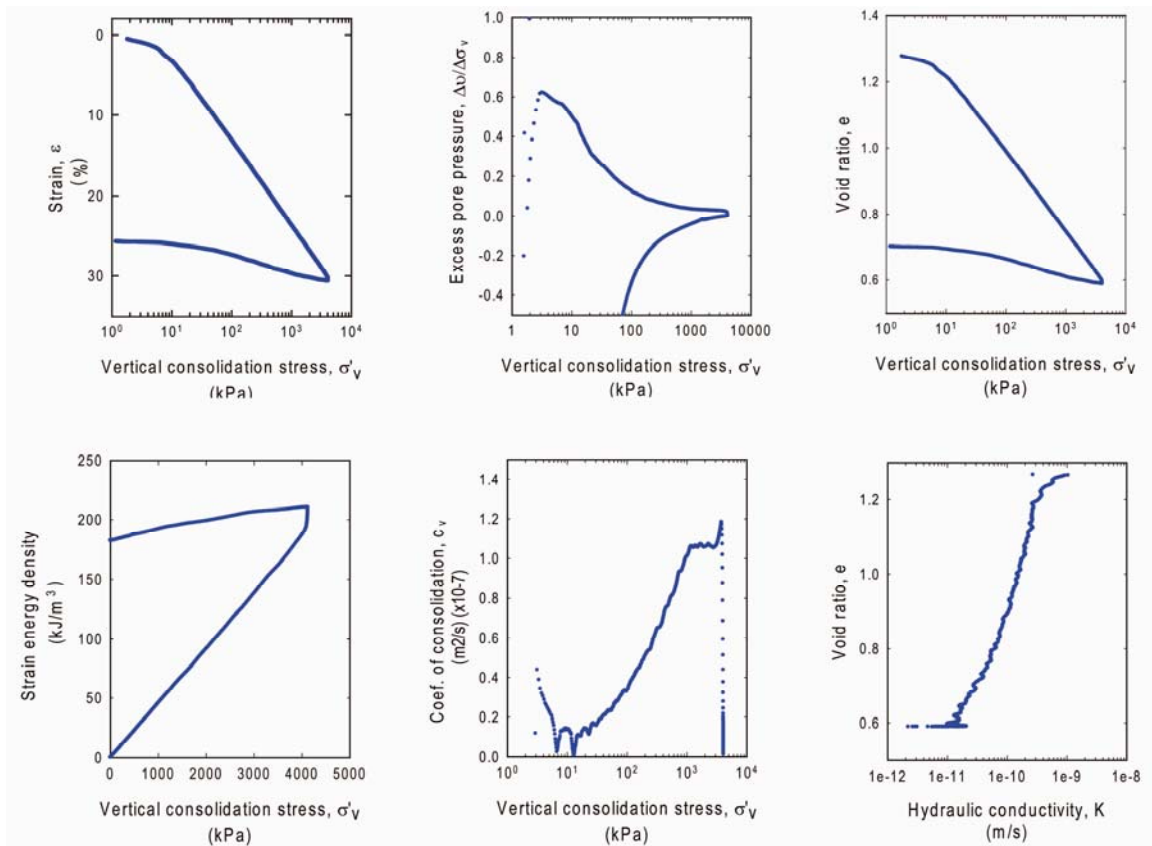


Figure A10: CRS040\_ut Consolidation Data

Remolded Boston Blue Clay from CRS039\_ut trimmings

## Appendix B

### *Grain Size Analysis*

#### METHODS

I conducted hydrometer grain size analyses at the University of Texas at Austin (UT) GeoMechanics Laboratory in accordance with ASTM D422-63 [*ASTM International*, 2003]. The actual CRS specimens were used as source material – each was dried, ground into the original grain size. I added water and deflocculant to separate out individual clay particles, agitated the slurry using a malt mixer, and brought it up to volume in a 1L graduated cylinder using deionized water. The hydrometer is lowered into the water-sediment suspension at doubling time intervals – 30 seconds, 1 minute, 2 minutes, 4 minutes, and through 1024 minutes (Figure B01). Measurements are continued in the morning and evening, until the plotted data are well into the clay-size particle range. The coarsest particles fall out immediately, reducing the density of the upper fluid-sediment mixture. Over time successively finer grains fall out of the suspension, further reducing the density and homogenizing the upper medium to a very clay-fluid suspension.

The two basic calculations made during a hydrometer analysis are the particle diameter at a specific time and depth and the percentage of the original sample mass still left in suspension. I calculate the particle diameter according to the following equation:

$$D = \sqrt{\frac{30\eta}{G_s - 1}} \sqrt{\frac{L}{t}}$$

Where:

D = equivalent sedimentation diameter of particle (millimeters)



$\eta$  = viscosity of water (grams seconds per square centimeter)

Gs= specific gravity of sediment

L = effective depth measured from water surface to center of gravity of hydrometer bulb (centimeters)

t = time measured from start of sedimentation (seconds).

The percentage of particles remaining in suspension finer than particle diameter, D, is

$$\%Finer = \frac{Gs}{Gs - 1} \times \frac{V}{M} \times \frac{Rh - B}{10}$$

Where

Gs= specific gravity of sediment

V = total water-sediment volume (1000 mL)

M= dry sample mass (grams)

Rh= corrected hydrometer reading of slurry mixture (grams per liter)

B = hydrometer reading of reference mixture of dispersing agent and distilled water (grams per liter).

## **SAMPLES**

I performed grain size analysis on the consolidated specimens of CRS016\_ut, CRS017\_ut and CRS018\_ut. Each specimen was dried at 110F and pulverized into fine grains.

## **RESULTS**

Plots for each experiment document the grain size – sand, silt and clay – versus % finer (Figure B02-B03)) and demonstrate all samples fall within the silty-clay

classification (60% clay +/- 10%, and 40% silt). CRS016\_ut, the non-MTD specimen at 75mbsf has 64% clay. CRS017\_ut, non-MTD at 126mbsf and CRS018\_ut, MTD-2 at 115mbsf, both have 58% clay content. Previous grain size analyses on the same core as CRS017\_ut is sourced from record grain size of 60%. Therefore I observe the coarsest grains within the MTD-2. Permeability results from the CRS tests combined with these grain size analyses indicate a general trend of decreasing permeability with increasing clay content (see main paper).

Project: CRS 017

Test Number: GS017

Boring: 1322B

Hydrometer

Tested by: CP, HES

Sample: 15H1

Type: 151H Fisher Brand

Test Date: 6/3/2009

Location: \_\_\_\_\_

Number: 98

Volume = 72 cm<sup>3</sup>

•Dispersing agent: Sodium

Assumed Specific Gravity: 2.78

Hr @ 1035 = 5.912 cm

Hexametaphosphate

Measured Dry Sample Mass: 48.42 g

Hr @ 1000 = 15.212 cm

•Dispersing agent not included

Measured Dispersing Agent Mass: 5.00 g

Meniscus = 0.8 g/L

in sample dry mass

Measurements				Constants		Results	
Elapsed Time (min.)	Susp'n Reading (g/L)	Water + Disp'nt Reading (g/L)	Temp. (°C)	Viscosity (g-s/cm <sup>2</sup> )	Effective Depth (cm)	% Finer (%)	Diameter (mm)
0.25	1035.0	1003.5	23.0	9.56669E-06	5.869327428	101.60	0.061526
0.5	1034.8	1003.5	23.0	9.56669E-06	5.922684951	100.96	0.043702
1	1034.4	1003.5	23.0	9.56669E-06	6.082757517	99.67	0.031317
1.5	1034.2	1003.5	23.0	9.56669E-06	6.136115039	99.02	0.025682
2	1034.0	1003.5	23.0	9.56669E-06	6.136115039	98.38	0.022241
4	1033.2	1003.5	23.0	9.56669E-06	6.349545127	95.80	0.015998
8	1032.2	1003.5	23.0	9.56669E-06	6.616332738	92.57	0.011548
16	1030.2	1003.5	23.0	9.56669E-06	7.149907958	86.12	0.008488
32	1029.6	1003.5	23.0	9.56669E-06	7.309980525	84.19	0.006069
64	1026.8	1003.5	23.0	9.56669E-06	8.056985834	75.15	0.004505
128	1024.8	1003.5	23.0	9.56669E-06	8.590561054	68.70	0.003290
256	1022.9	1003.5	23.0	9.56669E-06	9.097457514	62.58	0.002394
402	1021.4	1003.5	23.0	9.56669E-06	9.49763893	57.74	0.001952
1250	1019.0	1003.5	23.0	9.56669E-06	10.13792919	50.00	0.001144
1805	1017.2	1003.5	23.0	9.56669E-06	10.61814689	44.19	0.000974
2991	1016.3	1003.5	23.0	9.56669E-06	10.85825574	41.29	0.000765
5760	1014.6	1003.5	23.0	9.56669E-06	11.31179468	35.80	0.000563

Figure B1: Example Grain Size Analysis Data Sheet

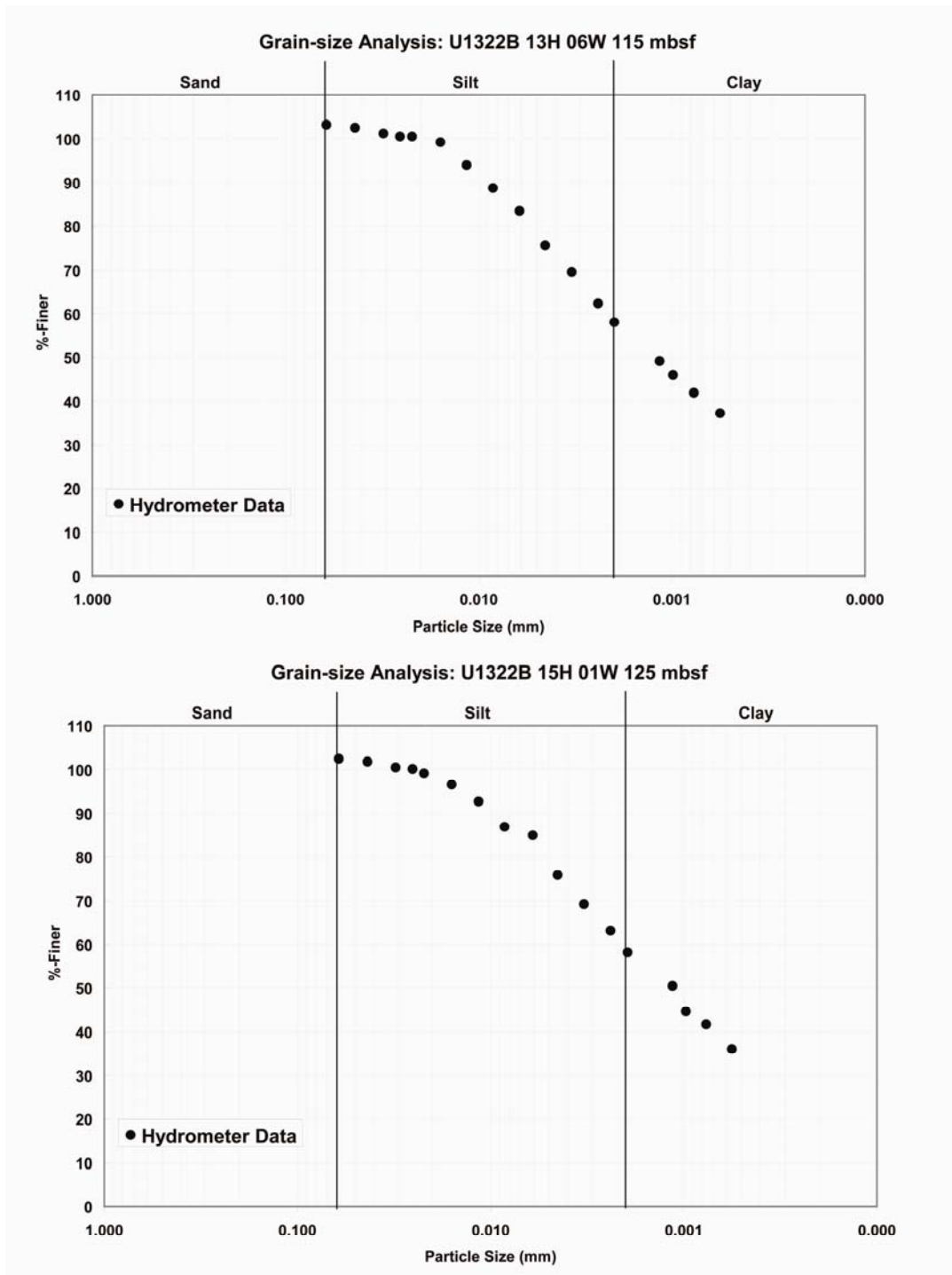


Figure B2: Non-MTD Grain Size Analysis

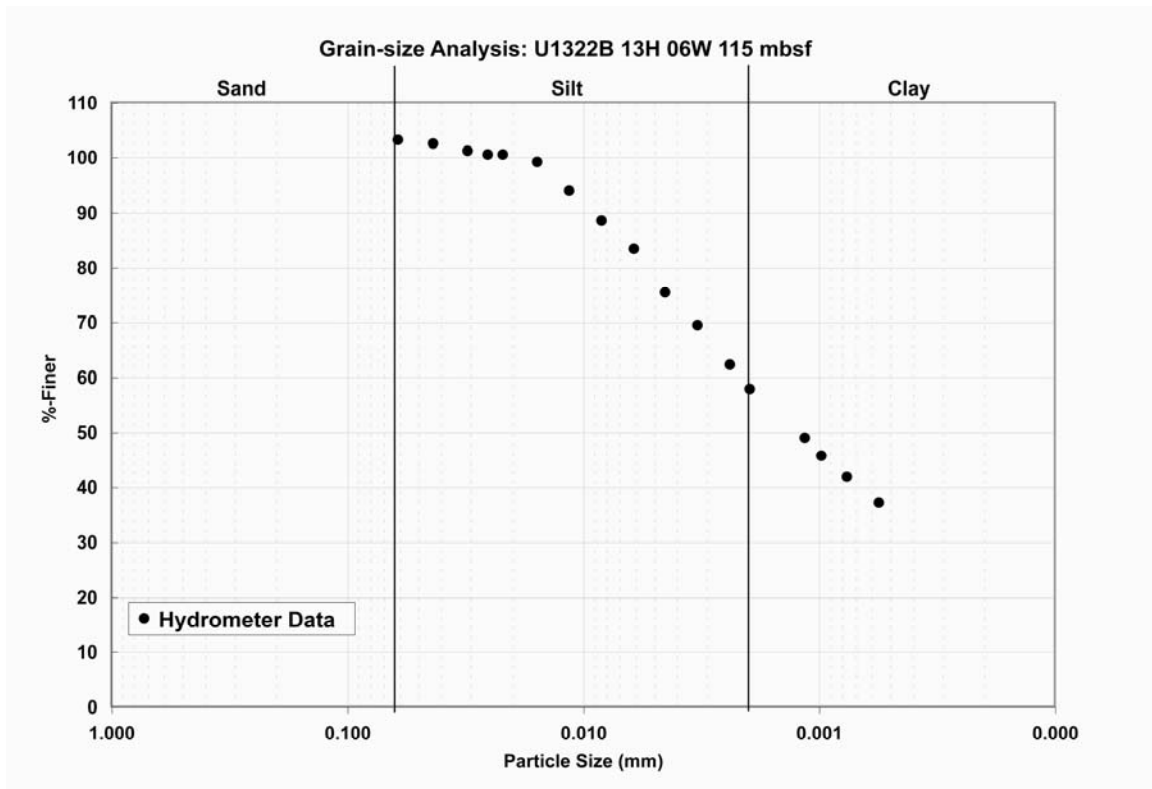


Figure B3: MTD-2 Grain Size Analysis

## **Appendix C**

### ***Computed Tomography Core Scans***

Cores were scanned using a medical CT scanner at the UT Department of Petroleum Engineering and UT High Resolution X-Ray CT Facility, and processed at the UT High Resolution X-Ray CT Facility. The medical CT scanner parameters are 1mm slices, 120kV, 100mA, and 4 second scan time (Figure C01). The X-Ray CT scanner parameters are 1mm slices, 450kV, 3mA, and 30 second scan time (Figure C02).

#### **MEDICAL SCANNER RESULTS**

Three cores were scanned using a medical CT machine. Two are from within MTD-2 at 104.5 (C01a) and 115mbsf (C01b); and the third is located immediately below MTD-2 at 126mbsf (C01c). The core located immediately below MTD-2 was also scanned using the X-Ray CT machine for comparison. The medical scanner distinguishes changing density within the core based on a gray scale within the image. The black sections within the cores C01b and C01c denote low density material – the blackest correspond to air – and the whiter areas denote high density material; this scale is reversed in core C01a due to processing change at the scanning facility. The shallower MTD-2 core shows high-angle banding, possibly corresponding to tilted bedding or sheared sediment. The deeper MTD-2 core has a series of black lines perpendicular to the cores length: multiple hairline fractures indicating a high degree of deformation. The non-MTD core has black zones indicating cracks have formed within the core, however this is attributed to dehydration and transportation – post coring sample degradation. Intact sections of this non-MTD core are very homogenous in color, and thus density, and show no deformation other than consolidation from geologic loading.

## **X-RAY SCANNER RESULTS**

Four cores were scanned using a X-Ray scanner. Two are located between MTD-1 and MTD-2 at 71.5mbsf (C02a) and 74.5mbsf (C02b). The third is located within MTD-2 at 115mbsf (C02c) and was also scanned with the medical CT machine. The fourth core (C02d) is from 211.7mbsf and represents non-MTD sediment. Like the medical scanner, the X-Ray scanner also distinguishes changing density on a gray scale with the black sections corresponding to air and the whiter areas denoting higher density material. Visual analysis of the cores between MTD-1 and MTD-2 shows some fracture from dehydration and post-sampling damage, however the intact sections are very homogenous. Like the medical CT scan, the X-Ray scan of the MTD-2 sample shows several fractures throughout the core (as black lines on the density scale), indicating this core has experienced a greater degree of deformation than the non-MTD cores. The deepest sample actually shows the least degree of deformation and is an extremely homogenous specimen, indicative of non-MTD sediments.

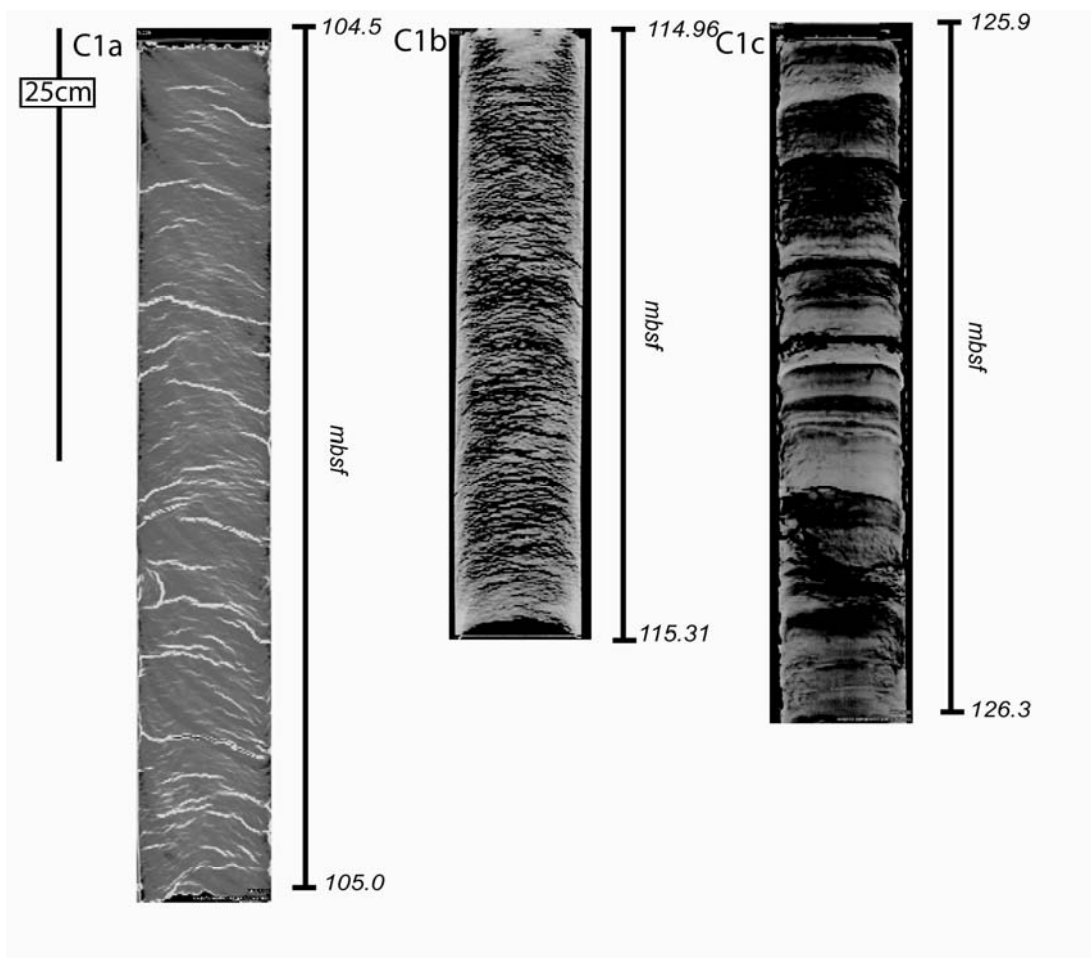


Figure C1: Medical CT Core Scans



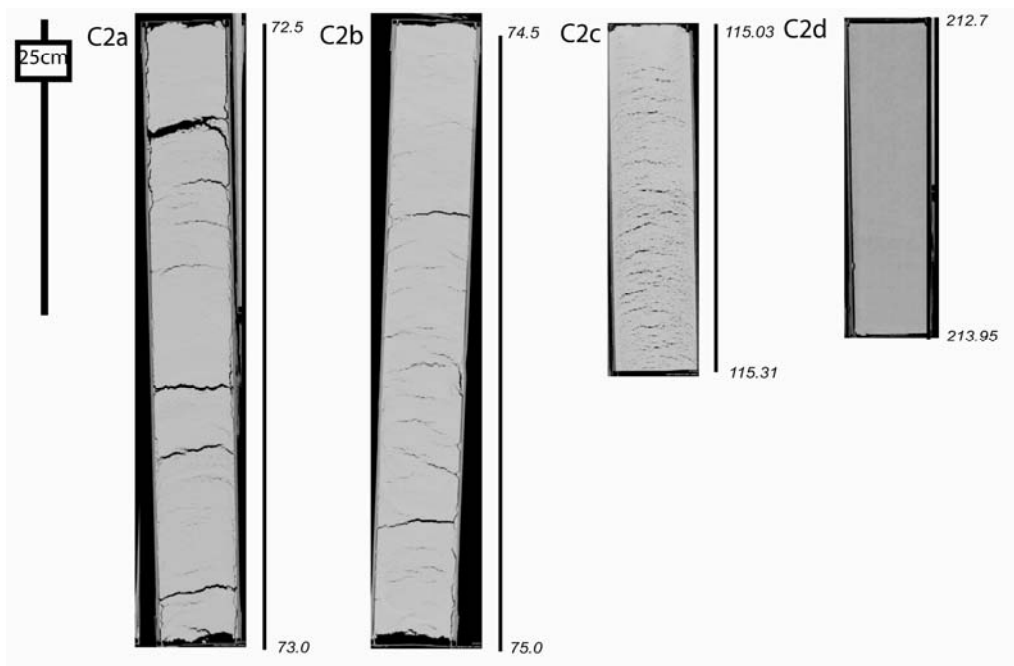


Figure C2: X-Ray CT Core Scans

## References

- ASTM International, 2003, Standard test method for one-dimensional consolidation properties of soils using controlled-strain loading (Standard D4186): In Annual Book of ASTM Standards, v. Vol. 04.08, p. Soil and Rock (I): West Conshohocken, PA (Am. Soc. Testing and Mater.), p. 530–535.
- Becker, D. E., et al. (1987), Work as a criterion for determining in situ and yield stresses in clays, *Canadian Geotechnical Journal*, 24, 549-564.
- Burland, J. B. (1990), On the compressibility and shear strength of natural clays, *Geotechnique*, 40(3), 329-378.
- Casagrande, A. (1936), The determination of the pre-consolidation load and its practical significance, 1st International Conference on Soil Mechanics, 60-64.
- Coleman, J. M., and D. B. Prior (1988), Mass wasting on continental margins, *Ann. Rev. Earth Planet. Sci.*, 16, 101-119.
- Das, B. M. (2002), *Principles of Geotechnical Engineering*, 5th ed., 589pp., Brooks/Cole Pacific Grove, CA
- Davis, D., et al. (1983), Mechanics of fold-and-thrust belts and accretionary wedges, *Journal of Geophysical Research*, 88(B2), 1153-1172.
- De Blasio, F. V., Elverhøi, A., Issler, D., Harbitz, C.B., Bryn, P. and Lien, R. (2004), Flow models of natural debris flows originating from overconsolidated clay materials *Marine Geology*, 213(1-4), 439-455.
- Dingle, R. V. (1977), The anatomy of a large submarine slump on a sheared continental margin (SE Africa), *Geological Society of London*, 134(3), 293-310.
- Dugan, et al. (2003) Consolidation Behavior, Stress, and Pressure of Sediments from ODP Site 1073, US Mid-Atlantic Continental Slope, *Earth and Planetary Science Letters*, 215, 13-26.
- Elverhøi, A., et al. (1997), On the origin and flow behavior of submarine slides on deep-sea fans along the Norwegian-Barents Sea continental margin, *Geo-Marine Letters*, 17, 119-125.
- Fayad, P. H. (1986), Aspects of the Volumetric and Undrained Behavior of Boston Blue Clay, 273 pp, MIT, Cambridge.

- Feeser, V., et al. (1993), Stress-regime-controlled yield and strength behavior of sediment from the frontal part of the Nankai accretionary prism, *Proc. Ocean Drill. Program Sci. Results*, 131, 261-271.
- Flemings, P. B., et al. (2008), Pore pressure penetrometers document high overpressure near the seafloor where multiple submarine landslides have occurred on the continental slope, offshore Louisiana, Gulf of Mexico *Earth and Planetary Science Letters*, 269/3-4 309-332.
- Gauer, P., et al. (2006), On numerical simulations of subaqueous slides: Back-calculations of laboratory experiments, *Norwegian Journal of Geology*, 86, 295-300.
- Hampton, M. A. (1975), Competence of Fine-Grained Debris Flows, *Journal of Sedimentary Petrology*, 45(4), 834-844.
- Hampton, M. A., et al. (1996), Submarine Landslides, *Reviews of Geophysics*, 34(1), 33-59.
- Hornbach, M. J., et al. (2008), Did a submarine landslide trigger the 1918 Puerto Rico tsunami, *Science of Tsunami Hazards*, 27(2).
- Hubbert, M. K., and W. W. Rubey (1959), Role of Fluid Pressure in Mechanics of Overthrust Faulting 1. Mechanics of Fluid-Filled Porous Solids and its Application to Overthrust Faulting, *Bulletin of the Geological Society of America*, 70, 115-166.
- Iverson, R. M., et al. (1997), Debris-Flow Mobilization from Landslides, *Ann. Rev. Earth Planet. Sci.*, 25, 85-138.
- Karig, D. E., and G. Hou (1992), High-Stress Consolidation Experiments and Their Geologic Implications, *J. Geophys. Res.*, 97(B1), 289-300.
- Kenney, T. C. (1964), Sea-Level Movements and the Geologic Histories of the Post-Glacial Marine Soils at Boston, Nicolet, Ottawa and Oslo, *Geotechnique*, 14(no. 3), 203-230.
- Lambe, T. W., and R. V. Whitman (1969), *Soil Mechanics*, 553pp., John Wiley & Sons, Inc., New York.
- Leroueil, S. et al., (1985), Discussion: Correlations Between Index Tests and the Properties of Remoulded Clays. W. D. Carrier III and J. F. Beckman, *Geotechnique*, 35(2), 223-226.
- Locat, J., and J. L. Homa (2002), Submarine landslides: advances and challenges, *Canadian Geotechnical Journal*, 39(1), 193-212.

- Long, H., Flemings, P.B., Germaine, J.T., Saffer, D. (2008), Data Report: Consolidation Characteristics of Sediments from IODP Expedition 308, Ursa Basin, Gulf of Mexico, *In Flemings, P.B., John, C. (Eds.), Proc. ODP, Sci. Results, 308*.
- Lucente, G. C., and G. A. Pini (2003), Anatomy and emplacement mechanism of a large submarine slide within a Miocene foredeep in the Northern Apennines, Italy: A field perspective, *American Journal of Science, 303*, 565-602.
- Major, J. J., and R. M. Iverson (1999), Debris-flow deposition: Effects of pore-fluid pressure and friction concentrated at flow margins, *GSA Bulletin, 111*(10), 1424-1434.
- Martinsen, O. J., and B. Bakken (1990), Extensional and compressional zones in slumps and slides in the Namurian of County Clare, Ireland, *Journal of the Geological Society, London, 147*, 153-164.
- Masson, D. G., et al. (2006), Submarine landslides: processes, triggers and hazard prediction, *Philosophical Transactions of the Royal Society - Mathematical Physical and Engineering Sciences, 364*(1845), 2009-2039.
- Mitchell, J. K. (1993), *Fundamentals of Soil Mechanics*, 422 pp., Wiley, New York, NY.
- Moscardelli, L., et al. (2006), Mass-transport complexes and associated processes in the offshore area of Trinidad and Venezuela, *AAPG Bulletin, 90*(7), 1059-1088.
- Olson, R. E. (1986), State of the Art: Consolidation Testing, *Consolidation of Soils: Testing and Evaluation, ASTM STP 892*.
- Piper, D. J. W., et al. (1997), Mass-Transport Deposits of the Amazon Fan, in *Proceedings of the Ocean Drilling Program, Scientific Results*, edited by R. D. Flood, Piper, D.J.W., Klaus, A., and Peterson, L.C., pp. 109-146.
- Pirmez, C., et al. (2004), Observations and Numerical Modeling of Debris Flows in the Na Kika Basin, Gulf of Mexico, in *Offshore Technology Conference*, Houston, Texas.
- Posamentier, H. W., and V. Kolla (2003), Seismic geomorphology and stratigraphy of depositional elements in deep-water settings, *Journal of Sedimentary Research, 73*(3), 367-388.
- Prior, D. B., et al. (1984), Depositional characteristics of a submarine debris flow, *J. Geol.*, 92, 707-727.
- Saffer, D. M. (2003), Pore pressure development and progressive dewatering in underthrust sediments at the Costa Rican subduction margin: Comparison with northern Barbados and Nankai, *Journal of Geophysical Research, 108*((B5)).

- Santagata, M., et al. (2005), Factors Affecting the Initial Stiffness of Cohesive Soils, *Journal of Geotechnical and Geoenvironmental Engineering*, 131(4).
- Sassa, S., et al. (2003), The Dynamics of Liquefied Sediment Flow Undergoing Progressive Solidification, in *Submarine Mass Movements and Their Consequences*, edited by J. Locat, Mienert, J., pp. 95-102, Kluwer Academic Publishers.
- Sawyer, D., Flemings, P.B., Dugan, B., and Germaine, J.T. (2009), Retrogressive failures recorded in Mass Transport Deposits in the Ursa Basin, Northern Gulf of Mexico, *Journal of Geophysical Research*.
- Sawyer, D. E., et al. (2007), Seismic Geomorphology, Lithology, and Evolution of the Late Pleistocene Mars-Ursa Turbidite Mini-Basin, Northern Gulf of Mexico, *AAPG Bulletin*, 91(2), 215-234.
- Schwab, W., et al. (1996), Sediment Mass-Flow Processes on a Depositional Lobe, Outer Mississippi Fan, *Journal of Sedimentary Research, Section A: Sedimentary Petrology and Processes*, 66(5 (September)), 916-927.
- Sheahan, T. C., and P. J. Watters (1997), Experimental Verification of CRS Consolidation Theory, *Journal of Geotechnical and Geoenvironmental Engineering*, 123(5).
- Shipp, R. C., et al. (2004), Physical Characteristics and Impact on Mass Transport Complexes on Deepwater Jetted Conductors and Suction Anchor Piles, paper presented at Proceedings of the Offshore Technology Conference, Houston, Texas, May3-6, 2007, OTC Paper #16751.
- Skempton, A. W. (1944), Notes on the Compressibility of Clays. *Q. J. Geol. Soc.*, 100, 119-135.
- Stow, D. A. A. (1986), Deep clastic seas, in *Sedimentary Environments and Facies*, edited by H.G. Reading, 399-444, Blackwell Scientific Publications, Oxford.
- Stump, B., and P. B. Flemings (2002), Consolidation State, Permeability, and Stress Ratio as Determined from Uniaxial Strain Experiments on Mud Samples from the Eugene Island 330 Area, Offshore Louisiana,, in *Pressure Regimes in Sedimentary Basins and Their Prediction*, edited by A. R. Huffman, Bowers, G.L., pp. 131-144.
- Tan, B., Germaine, J.T., and Flemings, P.B., (2006), Consolidation and strength characteristics of sediments from ODP Site 1244, Hydrate Ridge, Cascadia continental margin, paper presented at Proc. ODP, Sci. Results, 204.

- Tripsanas, E. K., et al. (2003), Structural Characteristics of Cohesive Gravity-Flow Deposits and a Sedimentological Approach on Their Flow Mechanisms, in *Submarine Mass Movements and Their Consequences*, edited by J. Locat, Mienert, J., pp. 129-136, Kluwer Academic Publishers.
- Weimer, P. (1990), Sequence Stratigraphy, Facies Geometries, and Depositional History of the Mississippi Fan, Gulf of Mexico, *AAPG Bulletin*, 74(4), 425-453.
- Weimer, P., and C. Shipp (2004), Mass Transport Complex: Musing on Past Uses and Suggestions for Future Directions, in *Offshore Technology Conference*, Houston, Texas.
- Winker, C. D., and J. R. Booth (2000), Sedimentary dynamics of the salt-dominated continental slope, Gulf of Mexico: integration of observations from the seafloor, near-surface, and deep subsurface, in *GCSSEPM Foundation 20th Annual Research Conference*, edited, pp. 1059-1086, Houston, TX.

## Vita

Hilary Elizabeth Strong was born and raised in La Jolla, California. In 2007, she earned a Bachelor of Science in Geology from the University of California Los Angeles. During her final year of undergraduate education, Hilary worked for a Geotechnical Engineering firm and became interested in the interdisciplinary field of geology and engineering. For her Masters of Science degree in Geology at the University of Texas at Austin, Hilary applied techniques from both fields to her research. In December of 2009, Hilary will begin a career at ExxonMobil Exploration Company in Houston, Texas as an Operations Geologist.

Permanent address: 6021 Bellevue Avenue, La Jolla, CA 92037

This thesis was typed by the author.